Microstructural, mechanical, and thermal characterization of constitutive layers in copper-steel functionally graded material manufactured via laser directed energy deposition

Romano, Tobia; Abdelwahed, Marawan; Bertolo, Virgínia; Cecotti, Tommaso; Skhosane, Samuel; Mahadevan, Gautham; Popovich, Vera; Hermans, Marcel; Taha, Mohamed A.; Pityana, Sisa

DOI
10.1016/j.matdes.2025.114329

Publication date
2025

Document Version
Final published version

Published in
Materials and Design

Materials & Design 256 (2025) 114329

Contents lists available at ScienceDirect

Materials & Design

journal homepage: www.elsevier.com/locate/matdes

Microstructural, mechanical, and thermal characterization of constitutive layers in copper-steel functionally graded material manufactured via laser directed energy deposition

Tobia Romano [a,b,*], Marawan Abdelwahed [c], Virgínia Bertolo [d], Tommaso Cecotti [a], Samuel Skhosane [e], Gautham Mahadevan [d], Vera Popovich [d], Marcel Hermans [d], Mohamed A. Taha [c], Sisa Pityana [e], Maurizio Vedani [a]

[a] Department of Mechanical Engineering, Politecnico di Milano, Milan, Italy
[b] Institute of Particle Physics and Accelerator Technologies, Riga Technical University, Riga, Latvia
[c] Design and Production Engineering Department, Faculty of Engineering, Ain Shams University, Cairo, Egypt
[d] Materials Science and Engineering, Delft University of Technology, Delft, the Netherlands
[e] Laser-Enabled Manufacturing Research Group, Council for Scientific & Industrial Research, Pretoria, South Africa

ARTICLE INFO

Keywords:
Additive manufacturing
Directed energy deposition
Functionally graded material
In-situ alloying
Copper

ABSTRACT

Copper-steel functionally graded materials combine the thermal conductivity of copper with the mechanical strength of steel. This study examines the microstructural, mechanical, and thermophysical properties of the constitutive layers of copper-4130 steel functionally graded material fabricated via laser directed energy deposition, considering four intermediate compositions: 100% 4130, 75% 4130 – 25% Cu, 50% 4130 – 50% Cu, and 25% 4130 – 75% Cu. It was observed that the amount of Cu-rich terminal liquid governs crack formation and backfilling during solidification, while Cu-Fe liquid phase separation and Marangoni convection within the melt pool generate macrostructures composed of alternating Cu- and Fe-rich phases. Increasing Cu content progressively enhances thermal diffusivity due to the formation of interconnected copper regions. The application of quenching and tempering treatments induced softening of Cu-containing samples due to Cu recrystallization and diffusion from supersaturated Fe-rich phases. Although solidification cracking was only observed in 75% 4130–25% individual samples, the analysis of a complete multilayer structure revealed that interlayer mixing causes local compositional variations, extending cracking susceptibility beyond this region. These findings provide insights into the key factors governing laser directed energy deposition of copper-steel functionally graded materials, supporting process optimization and predictive model development to enhance manufacturability.

1. Introduction

Metal multimaterial parts consist of different metallic materials strategically distributed to provide customized mechanical, physical, and chemical properties at specific locations [1]. Among possible material combinations, copper-steel structures couple the high electrical and thermal conductivity of copper with the structural strength of steel [2], making them suitable for applications in fields including power generation and transmission, nuclear industry, and die-casting [2–4]. Conventionally, copper-steel parts are produced using joining techniques such as laser welding [5], electron beam welding [6], metal arc welding [7], diffusion bonding [8], and vacuum brazing [9]. However, these methods often impose constraints on interface geometry and accessibility [10], making it challenging to fabricate complex components. Additionally, the need to produce and assemble multiple individual elements may result in high production costs and delivery times [11]. Thanks to its layer-by-layer building approach, additive manufacturing (AM) enables the creation of complex geometries while precisely controlling the spatial distribution of constituent materials within a part during the printing process [4]. This opens up the potential for fabricating monolithic multimaterial components, addressing the major limitations of conventional joining techniques.

* Corresponding author at: Department of Mechanical Engineering, Politecnico di Milano, 34 La Masa, Milan 20156, Italy.
E-mail address: tobia.romano@polimi.it (T. Romano).

https://doi.org/10.1016/j.matdes.2025.114329
Received 8 April 2025; Received in revised form 14 June 2025; Accepted 29 June 2025
Available online 30 June 2025

Research on AM of copper-steel multimaterials has mainly focused on powder bed fusion (PBF) [12,13] and directed energy deposition (DED) processes [14–16], using various heat sources (laser beam, electron beam, electric arc) and feedstock materials in both wire and powder form. PFB technologies generally offer higher resolution and the possibility of creating more intricate geometries compared to DED processes [17]. However, the need to generate a complete powder layer in each deposition step complicates the production of multimaterial structures, as special powder delivery systems are required for designs involving gradual variations between materials, such as in functionally graded materials (FGMs), and horizontal transitions within individual layers [18–20]. Moreover, separating dissimilar powders mixed in the powder bed at the end of the printing process is challenging and raises cross contamination and recycling issues [21]. On the other hand, DED methods are well-suited for multimaterial fabrication, because they deposit the feedstock materials only in specific areas according to the designed pattern. Therefore, these systems can be equipped with distinct delivery systems, like multiple hoppers or wire feeding devices, that can be selectively activated during the printing process to deposit the different materials in specified proportions and provide discrete or gradual compositional changes in all directions [22].

Several studies on DED of copper-steel multimaterials have shown the presence of interface cracks in direct junctions with sharp material variation [16,23]. Crack formation has been primarily attributed to the poor solubility between Fe and Cu, the wide solidification temperature range in the Fe–Cu system, and the large discrepancy in thermal conductivity and coefficient of thermal expansion, resulting in the accumulation of residual stress at the interface during the deposition process [23]. Liu and colleagues [17,20,24] also attributed crack formation to liquid metal embrittlement driven by the diffusion of liquid copper across the boundaries of the already solidified austenitic phase, promoted by its good wettability to these regions [25]. Alternatively, other researchers discussed the role of Cu-rich terminal liquid in the appearance of solidification cracks and possible healing mechanisms. For relatively low Cu contents, the terminal liquid is insufficient to compensate for the volumetric shrinkage, particularly in areas isolated by the already solidified austenite grains, and crack formation occurs due to lack of liquid replenishment and subsequent tensile strain generated at the end of solidification [14]. On the other hand, for high Cu contents, the abundant terminal liquid forms a continuous network in the material structure and no significant stress is generated during the final stage of solidification. Additionally, cracks that may have formed during the initial solidification of steel due to stresses induced by thermophysical property mismatch and rapid cooling can be healed by liquid copper backfilling aided by capillarity [12,26,27].

Two main strategies have been proposed to prevent cracking in copper-steel multimaterial structures produced by DED [23,26]. The first involves the introduction of an intermediate layer compatible with both Fe and Cu. Nickel alloys have been used for this purpose because Ni can form a solid solution with Fe over a wide compositional range (from ~5 wt% to ~60 wt% Ni content) and is fully soluble in Cu. Furthermore, the thermophysical properties of nickel alloys generally fall in the intermediate range between copper and steel, which helps mitigate the development of thermal stresses at the interface [23]. Several authors successfully suppressed interface crack formation by adding Ni-based intermediate layers in structures combining pure copper and copper alloys with different steel grades [23,28–31]. However, the use of buffer materials requires additional deposition steps and increases the complexity of the manufacturing process. The second strategy is based on the fabrication of FGM structures, which could prevent the generation of large residual stresses by providing a gradual transition of properties between the two materials [26]. Articek et al. [27] demonstrated this approach by fabricating test specimens using laser directed energy deposition (LDED) with powder blends with varying relative contents of Cu and H13 tool steel, as well as FGM samples with 10 wt% increments along the compositional gradient. They attributed the extensive presence of porosity and microcracks in the FGM structure to non-optimized processing parameters. Yadav et al. [26] produced FGM samples by LDED from pure copper and 304L stainless steel powders with 20 wt% Cu additions for every two deposited layers. They observed solidification cracks extending across multiple layers in the graded region, attributed to a continuous copper film resulting from the interaction between newly deposited material and underlying layers partially remelted by the laser at each deposition step. During the repeated heating and cooling cycles of the LDED process, thermal strain accumulated in the copper film, eventually causing its rupture and subsequent crack generation. In another study [14], they showed that cracking susceptibility in LDED of copper-304L stainless steel samples is governed by the amount of Cu-rich terminal liquid and the cooling rate during melt pool solidification, which in turn play a role in the mechanisms of liquid replenishment and crack backfilling.

Despite extensive research on the microstructure evolution during LDED of copper-steel multimaterials and the resulting mechanical properties [4,32], information regarding the thermophysical properties of the intermediate regions, where peculiar microstructures arise from the coexistence of immiscible phases, is still lacking. Addressing this gap is essential to elucidate the mechanisms governing solidification and stress development during the LDED process and better understand their impact on the performance of copper-steel FGM components. The prospect of developing adequate heat treatments for structures combining materials with very different melting points and transformation temperatures also remains an open question. Kremer et al. [33] had to find a compromise to stress relieve 316L-CuSn10 multimaterial parts produced by laser powder bed fusion (LPBF) while avoiding recrystallization in the CuSn10 regions. However, the treatment performed at relatively low temperature and short holding time (400 °C for 20 min) did not significantly improve the corrosion resistance of the samples, and further testing at 600 °C was recommended. In a recent study, Uhlmann and Saber [34] tested different aging treatments to improve the mechanical and electrical properties of CuCr1Zr combined with H13 tool steel in multimaterial samples fabricated by LPBF. However, the opportunity to develop a heat treatment effective for the H13 regions was not explored. Other works on LDED of multimaterials coupling copper with heat-treatable steel grades only considered the as-built condition [2,4,23,35].

The present study investigates the microstructural, mechanical, and thermophysical properties of the constitutive layers of a functionally graded structure manufactured from pure copper and heat-treatable AISI 4130 low-alloy steel powders, deposited by LDED in varying weight ratios using an in-situ alloying approach. The solidification and defect formation mechanisms are also explored for the different compositions, along with the response to standard heat treatments of 4130 steel.

2. Materials and methods

2.1. Feedstock powders and LDED process

Gas atomized pure copper (99.9 wt% Cu, 45–90 μm) and AISI 4130 steel (53–150 μm) feedstock powders were supplied by TLS Technik GmbH & Co. and Höganäs AB, respectively. The chemical composition of the 4130 powder (equivalent to 25CrMo4 and 1.7218 grades under European standards) is reported in Table 1. Among the alloying elements of 4130 steel, Cr, C, and Mo have a negligible solubility in Cu at room temperature [36–38]. Therefore, they are not expected to form

Table 1
Chemical composition (in wt.%) of pure copper and 4130 steel powders.

Powder	Cu	Cr	Mn	C	Si	Mo	O	Fe
Cu	>99.9	–	–	–	–	–	<0.1	–
4130	–	1.00	0.60	0.30	0.30	0.20	0.05	Bal.

significant solid solutions within the Cu-rich regions of the copper-steel samples. On the other hand, Mn and Si exhibit solubilities of ~2.6 wt% and ~4.5 wt% in Cu, respectively [39,40], and are thus expected to partially dissolve into the Cu-rich phase, forming solid solutions during solidification.

Individual blend composition samples were produced using an LDED system equipped with a KUKA AG robotic arm, an ytterbium fiber laser source with a maximum power of 3 kW, and multiple hoppers capable of simultaneously delivering up to four different powders. This setup provided precise control over each powder feed rate, enabling the in-situ production of distinct blend compositions by directly supplying the two powders in specified weight ratios into the melt region. Four nominal compositions with progressively increasing Cu content were considered, as indicated in the Fe-Cu equilibrium phase diagram of Fig. 1, calculated using Thermo-Calc software with TCFE12 and MOBFE7 Steel/Fe-alloy databases: 100 % 4130 (Fe_{100}), 75 % 4130 – 25 % Cu ($Fe_{75}Cu_{25}$), 50 % 4130 – 50 % Cu ($Fe_{50}Cu_{50}$), and 25 % 4130 – 75 % Cu ($Fe_{25}Cu_{75}$). Table 2 lists the processing parameters used in the LDED process. Further details on powder feed rate calibration are provided in Table S1 of the Supplementary Material. All the samples (Fig. 2(a)) were manufactured using the same experimental conditions and the relative powder feed rates were adjusted to achieve the four nominal compositions under examination. An additional FGM specimen was fabricated by sequentially depositing four layers for each intermediate composition using the same processing parameters as the individual blend composition samples, followed by two final layers of pure copper (Cu_{100}). The structure of the multilayer FGM sample is schematically illustrated in Fig. 2(b).

2.2. Calorimetry and thermodynamic modelling

A Setaram Themys One differential scanning calorimetry (DSC) analyzer was used to determine the main phase transformation temperatures for the individual blend compositions. For the analyses, samples of ~50 mg were extracted from the as-built cubes and heated to 1550 °C at a rate of 10 °C min^{-1}. Measurements were carried out in an inert atmosphere with an Argon flow rate of 50 ml min^{-1}. Experimental data were compared with thermodynamic simulations based on the CALPHAD method to index DSC peaks and support the definition of other minor phases. Simulations were run with Thermo-Calc software employing TCFE12 and MOBFE7 Steel/Fe-alloy databases.

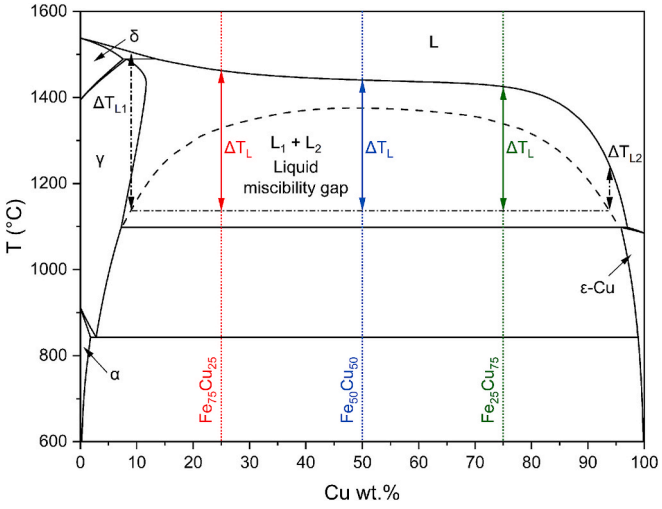

Fig. 1. Fe-Cu equilibrium phase diagram. The colored vertical lines correspond to the investigated compositions.

Table 2
LDED processing parameters.

Parameter	Fe_{100}	$Fe_{75}Cu_{25}$	$Fe_{50}Cu_{50}$	$Fe_{25}Cu_{75}$	Cu_{100}
Laser power (kW)	1	1	1	1	1
Laser scanning speed (mm min^{-1})	600	600	600	600	600
Laser spot size (mm)	2	2	2	2	2
Layer thickness (mm)	0.65	0.70	0.70	0.70	0.70
Standoff distance (mm)	12	12	12	12	12
Hatching distance (mm)	1	1	1	1	1
Argon shielding gas flow rate (l min^{-1})	15	15	15	15	15
Argon carrier gas flow rate (l min^{-1})	1.5	1.5	1.5	1.5	1.5
4130 powder feed rate (g min^{-1})	5.33	4.00	2.67	1.33	–
Cu powder feed rate (g min^{-1})	–	1.33	2.67	3.75	5.00

2.3. Microstructural and mechanical characterization

The chemical composition of the printed specimens was quantitatively determined through X-ray fluorescence (XRF) using a Panalytical Axios Max WD-XRF spectrometer and SuperQ5.0i/Omnian software for data processing. The results were then compared to nominal blend compositions calculated from the chemical composition of the feedstock powders.

The microstructure of as-built samples was characterized through optical and scanning electron microscopy (SEM). The printed cubes were sectioned along the building direction (z-axis), mounted in epoxy resin, ground with SiC abrasive papers up to 2000 grit, and sequentially polished with 3 μm and 1 μm diamond suspensions. The distribution of Cu- and Fe-rich regions in the blend composition specimens was initially examined by observing the polished sections with a Keyence VHX-5000 digital optical microscope and acquiring energy dispersive X-ray spectrometry (EDS) maps using a Zeiss Sigma 500 field-emission SEM. Specific microstructural features of steel regions were then highlighted through chemical etching performed with Nital 1 % reagent (1 vol% nitric acid and 99 vol% ethanol), while grain boundaries in copper regions were revealed using a solution prepared with 1 g $FeCl_3$, 25 ml HCl, and 70 ml distilled water. Phase and crystallographic orientation analyses were conducted through electron back scattered diffraction (EBSD) and X-ray diffraction (XRD). Prior to the analyses, the samples were sectioned along the building direction and polished to mirror-like surface following the same metallographic procedures described above. EBSD data were acquired using a Helios plasma focused ion beam SEM equipped with an AMETEK-EDAX camera and operating at a probe current of 3.2 nA and an accelerating voltage of 20 kV, with a tilt angle of 70° and a step size of 0.35 μm. Raw data were postprocessed using EDAX OIM Analysis 8 software to construct transverse inverse pole figure (IPF) maps, displaying the crystallographic orientation along the building direction, as well as phase maps and grain size distribution diagrams. Grains were defined with a minimum grain boundary misorientation angle of 5° and a minimum size of 5 pixels. XRD measurements were performed using a Bruker D8 Advance diffractometer, operating at 40 kV voltage and 40 mA current with Co Kα radiation. Diffraction spectra were collected over a 2θ range of 40–130° with 0.04° step size and 1 s counting time per step and indexed using the DIFFRAC. EVA 7.1 software package.

Vickers microhardness and indentation plastometry tests were conducted to evaluate the mechanical properties of the investigated materials. A Future-Tech FM-700 instrument was used for microhardness testing. Given the inhomogeneous microstructure of the samples, which featured distinct softer Cu-rich areas and harder Fe-rich areas, a relatively high load of 1 kgf was initially applied for a dwell time of 15 s to generate an indent encompassing both regions, thus providing an overall estimate of the material microhardness. The load was then reduced to 25

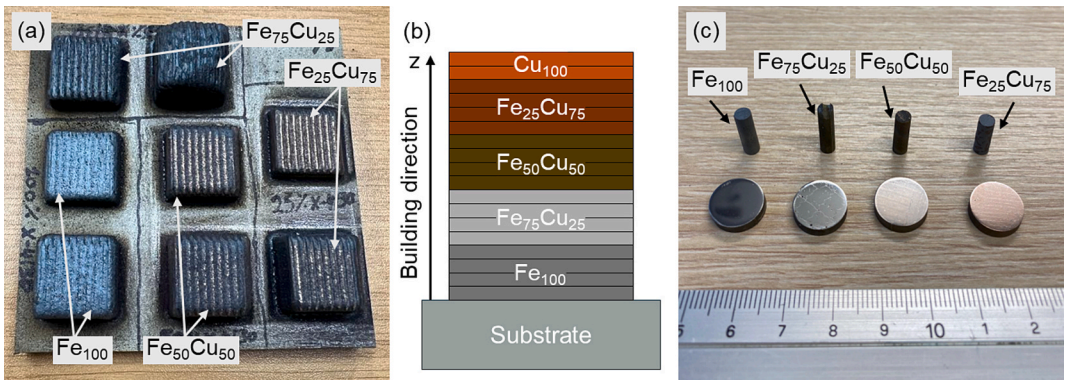

Fig. 2. View of individual blend composition samples fabricated by LDED (a), schematic of FGM sample (b), and specimens for dilatometry and thermal diffusivity measurements (c). The z-axis indicates the building direction.

gf to determine the microhardness of individual areas. The deformation characteristics and plastic properties of printed samples were analyzed by profilometry-based indentation plastometry (PIP) using a Plastometrex PLX-Benchtop device. The instrument was equipped with a spherical indenter with a radius of 1 mm, a linear variable differential transformer (LVDT) to measure the displacement during indentation, and a contact profilometer for capturing indent profiles. The tests were conducted under strain control, applying a progressively increasing load until reaching a penetration depth of ~200 μm, corresponding to a true plastic strain of 20 %. The true plastic strain is defined as the ratio between the penetration depth and the indenter radius. During each test, the load was applied at the same location in three discrete steps, increasing the peak load at each step, and the indent profile was measured after each loading step. After each measurement, the software runs an integrated inverse iterative finite element computation to fit the indent profile with Voce hardening parameters (yield stress σ_Y, saturation stress σ_S, and characteristic strain ε_0), generating a true stress–strain relation described by Equation (1).

$$\sigma = \sigma_S - (\sigma_S - \sigma_Y)e^{-\varepsilon/\varepsilon_0} \tag{1}$$

σ is the true stress and ε is the true strain [41]. The true stress–strain data are then converted into a nominal stress–strain curve, with the Young's modulus of the material specified as an input parameter before starting the test. The steel database integrated into the software was used for the Fe_{100} specimen, assuming a Young's modulus of 200 GPa. For specimens with blend compositions, the Young's modulus was estimated applying the rule of mixtures, based on representative values for steel (200 GPa) and copper (115 GPa). Brinell hardness was also included in the test outputs. Three measurements were performed on each sample, and the indent morphology was later examined with optical and SEM microscopy.

Optical micrographs of the FGM sample were collected along the building direction after sectioning and polishing following the same metallographic procedures described above. Images were acquired using both coaxial illumination and a combination of ring and coaxial lighting to enhance the contrast between intermediate layers with varying Cu and Fe contents. The local chemical composition of the constitutive layers of the FGM structure was qualitatively assessed through EDS area analyses. Additionally, the microhardness variation along the compositional gradient was determined with a test load of 1 kgf and a dwell time of 15 s.

2.4. Dilatometry and thermal diffusivity measurements

Standard cylindrical (0.4 mm diameter, ~10 mm length) and disk-shaped (12.7 mm diameter, ~1.5 mm thickness) specimens for dilatometry and laser flash analysis (LFA), respectively, were extracted from printed cubes by electrical discharge machining, as shown in Fig. 2(c). Since microstructural anisotropy is expected to influence the properties of parts fabricated by LDED, measurements in multiple directions would be necessary for a comprehensive characterization of their thermal behavior. However, due to the limited number of available cubes, only samples with the longitudinal axis aligned parallel to the building direction could be machined.

Dilatometry experiments were performed under vacuum (10^{-2} mbar) by applying a heating ramp of 3 °C min^{-1} to a peak temperature of 900 °C. A Linseis L75 vertical dilatometer equipped with an LVDT encoder was employed to measure the sample length variation during the analysis. The linear coefficient of thermal expansion (CTE) was calculated at different temperatures using Equation (2) [42].

$$\alpha = \frac{1}{l_1}\frac{l_2 - l_1}{T_2 - T_1} \tag{2}$$

$l_2 - l_1$ is the measured change in sample length due to temperature variation from T_1 to T_2. Temperature increments of 25 °C were used in the calculation to minimize the effect of instantaneous temperature fluctuations during measurement and obtain a more accurate representation of the CTE trend as a function of temperature.

Thermal diffusivity measurements were performed under vacuum conditions (~$1.2 \cdot 10^{-2}$ mbar), using a Linseis LFA 100 instrument equipped with a laser source operating at 350 V and 1 ms pulse duration. Both faces of the disks were polished up to 6 μm diamond suspension and coated with a thin graphite layer to ensure effective laser absorption during testing. A heating ramp was applied at a nominal rate of 5 °C min^{-1} up to 900 °C, and three thermal diffusivity values were recorded at intervals of 50 °C, with a tolerance of ±10 °C. For comparison, an additional measurement was conducted on a reference sample extracted from an annealed pure copper (>99.99 % Cu) wrought bar under the same experimental conditions. After completing the first cycle of measurements, the samples were allowed to cool slowly to room temperature inside the vacuum furnace. Although no active temperature control was applied at this stage, slow cooling was ensured by the bulky graphite sample holder that housed the disks during testing. Therefore, the microstructure of the samples likely approached the equilibrium conditions after cooling, compared to the initial microstructure resulting from rapid cooling during the LDED process. A second heating cycle was then applied with the same experimental parameters to evaluate the effect of these microstructural changes on the thermal diffusivity of the samples.

2.5. Heat treatment

To evaluate the response of different blend compositions to heat treatment, Fe_{100} and $Fe_{50}Cu_{50}$ samples were subjected to two different heat treatments based on previous studies on AM of 4130 steel [43,44]. $Fe_{25}Cu_{75}$ was not included in these analyses, as heat treatments designed

for 4130 steel were expected to have a limited impact on its mechanical properties due to the high Cu content. The first treatment, quenching and tempering (Q + T), involved an initial annealing step at 850 °C for 1 h, followed by water quenching and tempering at 550 °C for 1 h. In the second treatment, direct tempering (DT), a tempering cycle at 550 °C for 1 h was applied directly to as-built samples, considering the potential similarity between the microstructures resulting from the high cooling rates in LDED and conventional quenching.

The microstructure of heat-treated parts was characterized through optical and SEM microscopy complemented with XRD using the same setups and procedures already described for the corresponding as-built materials. Additional Vickers microhardness and indentation plastometry measurements were also performed to evaluate the effect of heat treatments on the mechanical properties.

3. Results and discussion

3.1. Macrostructure morphology and solidification mechanisms

Fig. 3 shows cross-sectional views of the fabricated samples along the building direction (z-axis), highlighting the distribution of distinct Cu- and Fe-rich macroareas, which appear orange and gray, respectively, in the $Fe_{75}Cu_{25}$, $Fe_{50}Cu_{50}$, and $Fe_{25}Cu_{75}$ blend compositions.

The Fe_{100} sample consists of macrodomains oriented toward the center of the melt pools, as highlighted in the inset of Fig. 3(a). This feature is typical of parts produced by LDED, where grains tend to grow perpendicular to the melt pool boundaries due to steep thermal gradient and directional heat flow toward the already solidified material [42]. This behavior is further evidenced in the $Fe_{75}Cu_{25}$ sample by the presence of Cu-rich fibrous fragments stretching along the grain growth direction in the melt pool core regions, as shown in the inset 2 of Fig. 3(b). Zafari and Xia [45,46] attributed the development of a similar macrostructure in Fe-20Cu (vol.%) parts produced by LPBF to liquid phase separation occurring within the miscibility gap in the Fe-Cu system (Fig. 1). During the LDED process, the initial liquid L is undercooled into the metastable miscibility gap due to rapid cooling and separates into two distinct liquid phases (Fe-rich L_1 and Cu-rich L_2). For a given undercooling ΔT_L, L_1 experiences a higher degree of undercooling (ΔT_{L1}) compared to L_2 (ΔT_{L2}), as depicted in Fig. 1. Therefore, L_1 solidifies first and pushes L_2 into the regions between the already formed austenitic grains [45], resulting in irregularly shaped Cu-rich macrosegregation embedded in the steel matrix after complete solidification. The aligned fiber morphology observed in the core regions of the melt pools resulted from directional solidification driven by the thermal gradient and heat flow. Munitz [47] showed that the large miscibility gap in the Fe-Cu system induces the formation of copper fiber arrays regularly distributed within an Fe matrix. However, the relatively high growth rate during LDED likely caused the solidification front to break into non-steady state arrangements of irregular Cu-rich fiber fragments in the core region of the melt pools. The even faster solidification experienced at the melt pool boundaries due to direct contact with the underlying solid layers caused spheroidization and subsequent dispersion of copper droplets, as shown in the inset 1 of Fig. 3(b).

While no obvious defects were found in Fe_{100} parts, indicating appropriate processing parameters for the base steel, the $Fe_{75}Cu_{25}$ sample exhibited several large cracks extending through the entire part (Fig. 3(b)), along with large round pores probably caused by gas trapped in the molten material or to the boiling of low-melting Cu phases during the LDED process, induced by the relatively high laser power input. Crack formation can be primarily attributed to large thermal stresses arising from rapid cooling, repeated thermal cycles, and inhomogeneity in material structure and thermophysical properties. EDS estimated Fe and Cu contents of ~85 wt% and ~93 wt% in the matrix and dispersed particles, respectively, revealing the formation of a heterogeneous macrostructure consisting of distinct regions with significantly different thermal conductivity and expansion behavior. A slightly higher Mn content was measured in Cu-rich domains (~1.2 wt%) compared to the Fe-rich matrix (~0.5 wt%), consistent with its partitioning behavior as predicted by phase equilibrium diagrams [39,48]. While an even distribution of Si in Fe- and Cu-rich phases could be expected based on thermodynamic data [40,49], its low concentration in 4130 steel composition prevented clear detection by EDS. A Cr content of ~2.5 wt % was observed only in Fe-rich regions, given its negligible solubility in Cu [36]. Similar trends were observed in the local composition analysis

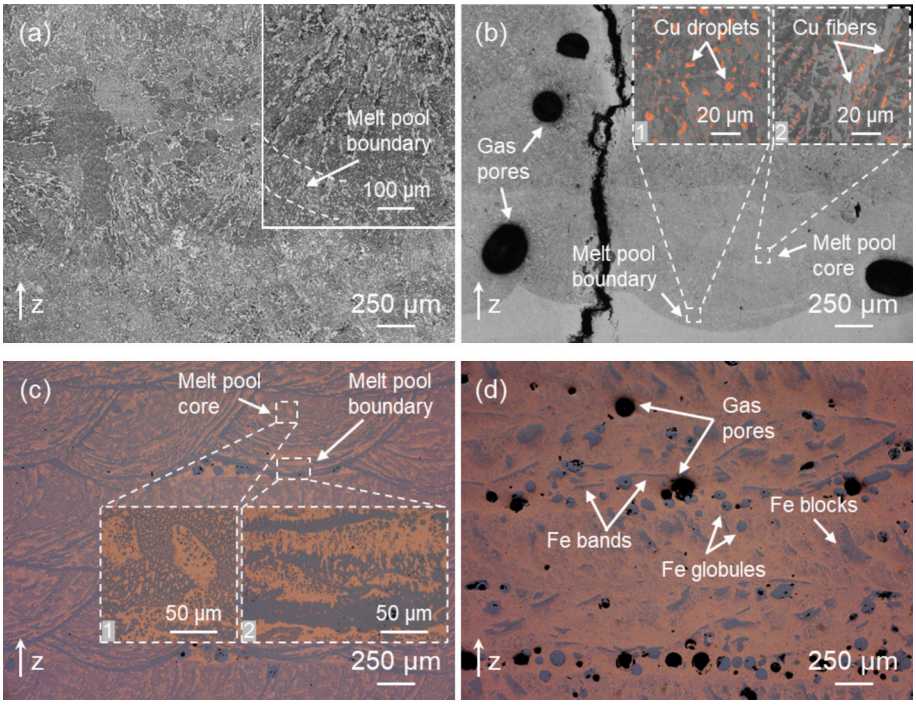

Fig. 3. Optical micrographs illustrating the macrostructure morphology of Fe_{100} (a), $Fe_{75}Cu_{25}$ (b), $Fe_{50}Cu_{50}$ (c), and $Fe_{25}Cu_{75}$ (d) samples. Fe-rich regions appear gray, while Cu-rich regions appear orange.

of the other blend composition samples. The presence of cracks filled with copper, either partially or fully (Fig. 4), suggests that liquid copper penetration occurs during the final stage of solidification, driven by capillarity action. In $Fe_{75}Cu_{25}$, only the thinnest microcracks can be healed by the copper veins due to the limited amount of Cu-rich terminal liquid (Fig. 4(a)), while larger cracks are only partially filled, as evidenced by the EDS maps in Fig. 4(b). Insufficient liquid replenishment may also have caused the tearing of local copper films that can form during solidification due to Cu accumulation at the grain boundaries of the already solidified austenitic phase [14]. At the end of solidification, contraction of the copper film constrained by the surrounding solid steel generates tensile stresses that can cause its rupture if the available terminal liquid is insufficient to compensate for volume shrinkage. Strain accumulation in the copper film is also promoted by the repeated heating and cooling cycles during LDED [26]. This mechanism of copper film tearing may explain the presence of Cu deposits occasionally observed on both sides of large macrocracks, as highlighted in Fig. 4(a).

The $Fe_{50}Cu_{50}$ sample consists of alternating Fe- and Cu-rich bands (Fig. 3(c)), resulting from liquid phase separation and material transfer within the melt pool driven by Marangoni convection. During the LDED process, the temperature at the center of the melt pool surface is higher than at the edges [50], creating a surface tension gradient that drives the liquid outward. Meanwhile, gravity causes the liquid to flow toward the bottom of the melt pool, generating a circular flow that produces the observed morphology, influenced by the immiscibility between the two distinct liquid phases. The schematic of Marangoni convection is illustrated in Fig. 5(a). Elongated stripes form at the melt pool boundaries, as highlighted in the inset 2 of Fig. 3(c), because the swirling macrostructure is frozen due to rapid solidification in regions directly in contact with the cold material underneath. On the other hand, the core of the melt pools exhibits blocky shapes, either consisting of an Fe-rich matrix with dispersed Cu-rich particles or a Cu-rich matrix with dispersed Fe-rich particles, as shown in the inset 1 of Fig. 3(c). In these regions, the lower cooling rate facilitates Cu and Fe separation, resulting in rounded morphologies that minimize the contact surface area between the immiscible phases. The inhomogeneity in cooling rates across the melt pool [51] can also explain the presence of both dendritic and globular Fe-rich structures at the bottom and top of Cu-rich bands, respectively, observed at the base of the melt pools (Fig. 5(b)). In the lower region, the high cooling rate results in dendrites growing above the Fe-rich band perpendicular to the melt pool boundary and parallel to the thermal gradient and heat flow [52]. The motion of the Cu-rich phase, which was still liquid after steel solidification, may have caused the dendrites to detach from the underlying Fe-rich band, resulting in the isolated dendrites highlighted in the EDS maps of Fig. 5 (b). The local cooling rate (C_R) was estimated to be $\sim 2.40 \times 10^5$ °C s^{-1}, based on secondary dendrite arm spacing (SDAS) analysis, as described in Section 2 of the Supplementary Material. This cooling rate is significantly higher than that reported for steel and Cu-Fe alloys processed by LDED under comparable experimental conditions [51,53], likely due to the close contact with the underlying consolidated material and the high Cu content in the area where dendrites formed. In contrast, the literature values refer to global cooling rates during the LDED process. The upper region of Cu-rich bands is dominated by Fe-rich globules due to slower cooling, which favored rounded morphologies with lower surface energy, as previously discussed for the core section of the melt pools.

Some backfilled microcracks penetrating through Fe-rich bands were observed in the analyzed sections, as highlighted in Fig. 5(b). Compared to the $Fe_{75}Cu_{25}$ system, the large amount of terminal liquid in $Fe_{50}Cu_{50}$ could heal the microcracks formed during the early stages of solidification by a backfilling mechanism, as reported in previous studies on LDED of copper-steel multimaterials [26,27].

When examined at progressively smaller length scales, the macrostructure of $Fe_{50}Cu_{50}$ sample displays a recursive pattern with copper and steel alternating as matrix and dispersed phase. This is illustrated in the representative SEM images of Fig. 6(a) taken at increasing magnifications in back scattered electron (BSE) mode, where Fe-rich areas appear darker and Cu-rich areas appear lighter. This hierarchical organization arises from primary and secondary phase separation mechanisms [54], driven by the immiscibility between Fe and Cu and the high cooling rate of the LDED process. As already discussed for the $Fe_{75}Cu_{25}$ system, the initial liquid L undergoes primary phase separation when undercooled within the miscibility gap, with the generation of distinct Fe- and Cu-rich liquid phases (L_1 and L_2, respectively). Upon further cooling, L_1 tends to follow the boundaries of the miscibility gap [54], gradually expelling solute atoms as the equilibrium concentration decreases (Fig. 1). Therefore, a secondary Cu-rich liquid forms from the secondary phase separation of L_1 and subsequently solidifies into finely dispersed precipitates, as depicted in the BSE micrograph at higher magnification in Fig. 6(a). An Fe-rich secondary liquid is also generated by L_2 decomposition through a dual mechanism, resulting in Fe-rich particles dispersed within Cu-rich macroareas (Fig. 6(b)). EDS measurements revealed a very high Cu content in Fe-rich bands (~12 wt%), attributable to the rapid solidification experienced by the largely undercooled L_1 during the LDED process. On the other hand, Cu-rich bands displayed a limited Fe content (~3.6 wt%), possibly because the lower degree of undercooling allowed for extensive diffusion of solute atoms before complete solidification. Although not directly observable at these magnifications, nano-sized precipitates can also result from Cu and Fe ejection from supersaturated solid phases, as reported by Yadav et al. [26] for Cu-304L multimaterial parts manufactured by LDED with the same blend composition.

In the $Fe_{25}Cu_{75}$ sample, the Cu-rich phase forms a continuous matrix due to its higher proportion in the blend composition (Fig. 3(d)). As observed for $Fe_{50}Cu_{50}$, the Fe-rich regions mainly appear as globular particles in the core of the melt pools and as elongated bands at the base, as a result of primary liquid phase separation, Marangoni convection, and the heterogeneous cooling rate across the melt pool. Despite the limited Fe content in the mixture, Marangoni motion promotes the collision and coalescence of isolated Fe-rich droplets formed by primary

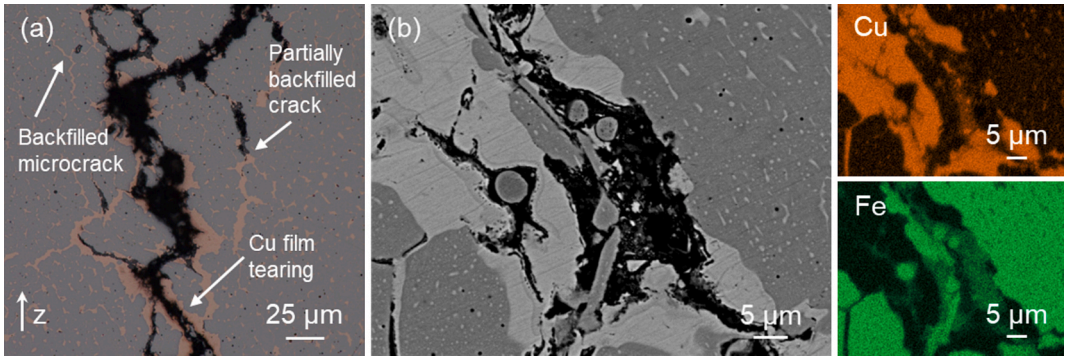

Fig. 4. Solidification cracks in $Fe_{75}Cu_{25}$ sample (a) and EDS maps of the cracked region (b).

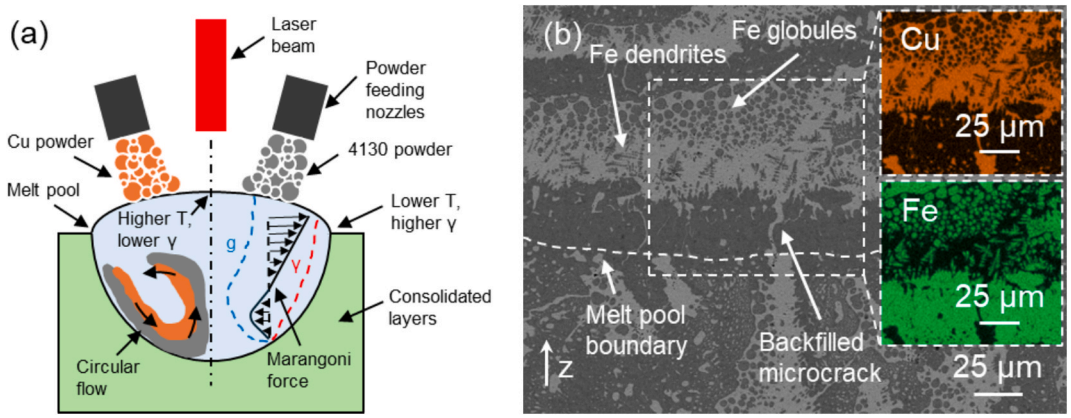

Fig. 5. Schematic of Marangoni convection (a) and interlayer region of $Fe_{50}Cu_{50}$ sample with corresponding EDS maps (b). Marangoni force distribution arises from the combined effects of surface tension gradient (γ) and gravity (g).

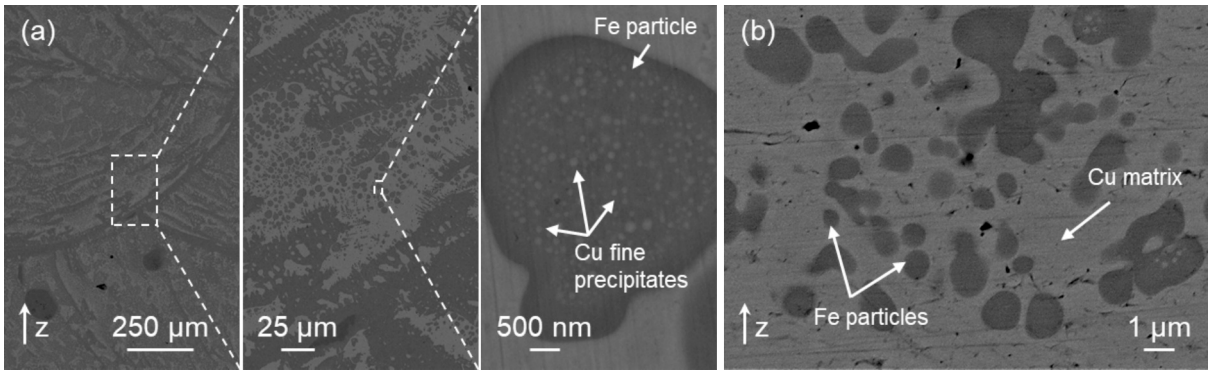

Fig. 6. Recursive macrostructure of $Fe_{50}Cu_{50}$ sample (a) and detail of Fe particles dispersed in Cu-rich macroareas (b).

liquid phase separation [55], leading to the development of macroscopic Fe-rich areas. In the boundary regions of the melt pool, rapid solidification prevails over surface tension effects, giving rise to stripe morphologies, as evidenced in Fig. 7. In contrast, the slower cooling rate in the core regions favors the formation of blocky shapes. The Fe-rich dendrites observed near these regions likely grew from Fe-rich bands and blocks and subsequently detached due to the motion of the Cu-rich liquid. The slightly higher local cooling rate estimated from the SDAS ($\sim 3.90 \times 10^5$ °C s^{-1}) compared to $Fe_{50}Cu_{50}$ is attributable to the increased Cu content. As discussed for $Fe_{25}Cu_{75}$, the prominent round pores observed throughout the sample cross-section (Fig. 3(d)) may have originated from gas entrapment or Cu boiling during the LDED process.

The results of XRF analysis (Fig. S1 in Supplementary Material) confirm that the chemical composition of the printed parts is consistent with the nominal values.

3.2. Phase analysis

Fig. 8(a) shows the XRD patterns of the as-built samples. The peaks labelled as α/α' can be attributed to ferrite/partially tempered martensite, resulting from the high cooling rates and repeated heating cycles during the layerwise deposition process. Although Thermo-Calc calculations indicated that the base steel undergoes martensitic

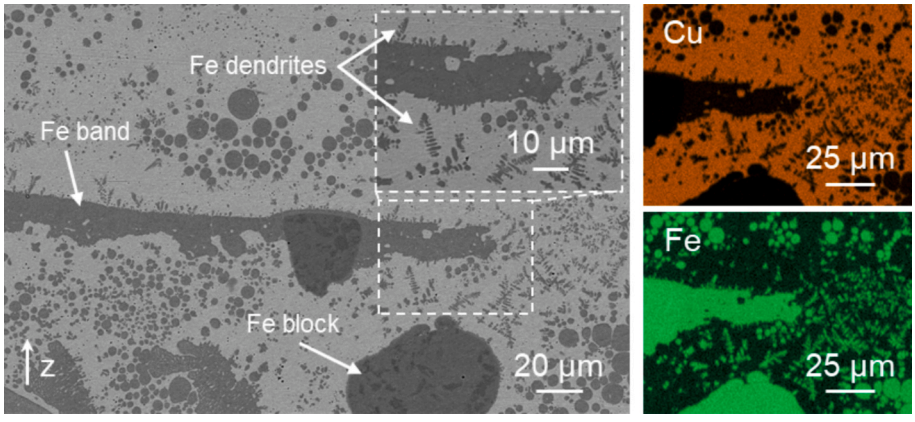

Fig. 7. Morphology of Fe-rich regions in $Fe_{25}Cu_{75}$ sample and corresponding EDS maps.

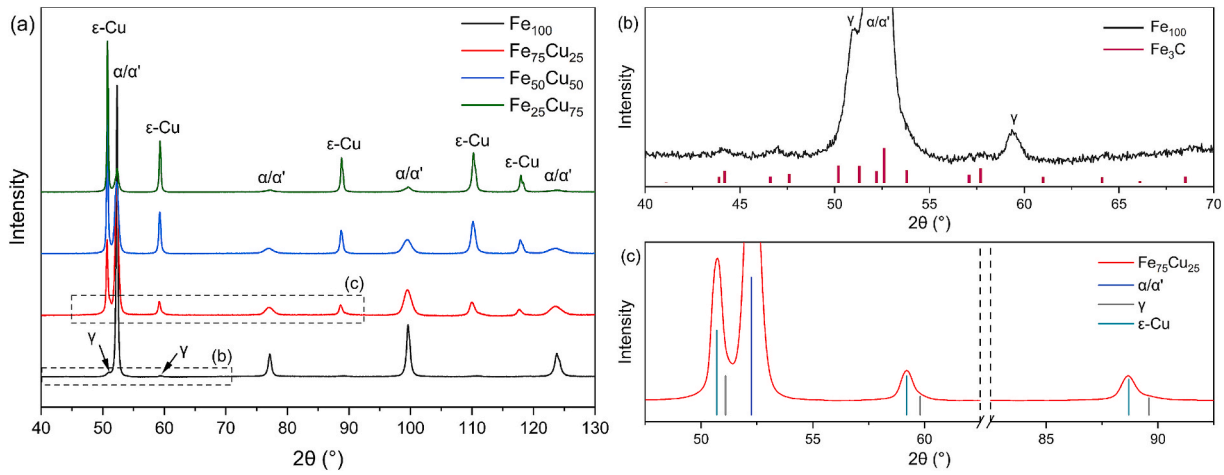

Fig. 8. XRD patterns of as-built samples (a) and zoomed-in sections of Fe_{100} (b) and $Fe_{75}Cu_{25}$ (c) diagrams.

transformation between the start temperature (M_s) of ~391 °C and the finish temperature (M_f) of ~309 °C, peaks corresponding to the austenite phase (γ) were detected in Fe_{100} and $Fe_{75}Cu_{25}$ (Fig. 8(b-c)). Austenite peaks are not clearly visible in $Fe_{50}Cu_{50}$ and $Fe_{25}Cu_{75}$ due to the overlapping signals from γ and ε-Cu phases, having similar lattice constants [56]. Retained austenite can be primarily attributed to the strain generated by the volumetric expansion associated with γ → α/α' phase change, which hindered further conversion during cooling and resulted in incomplete martensitic transformation. Repeated heating cycles during the LDED process may also have partially reversed the martensite in the previously deposited layers, contributing to the presence of γ in the form of reversed austenite.

Fig. 9 shows the heat flow curves obtained from DSC measurements during the heating stage, along with the corresponding phases predicted by Thermo-Calc simulations. The experimental results align well with equilibrium data, although the tests were conducted applying a finite heating rate of 10 °C min^{-1}. The broad exothermic peak observed in the first section of the thermograms is attributed to martensite

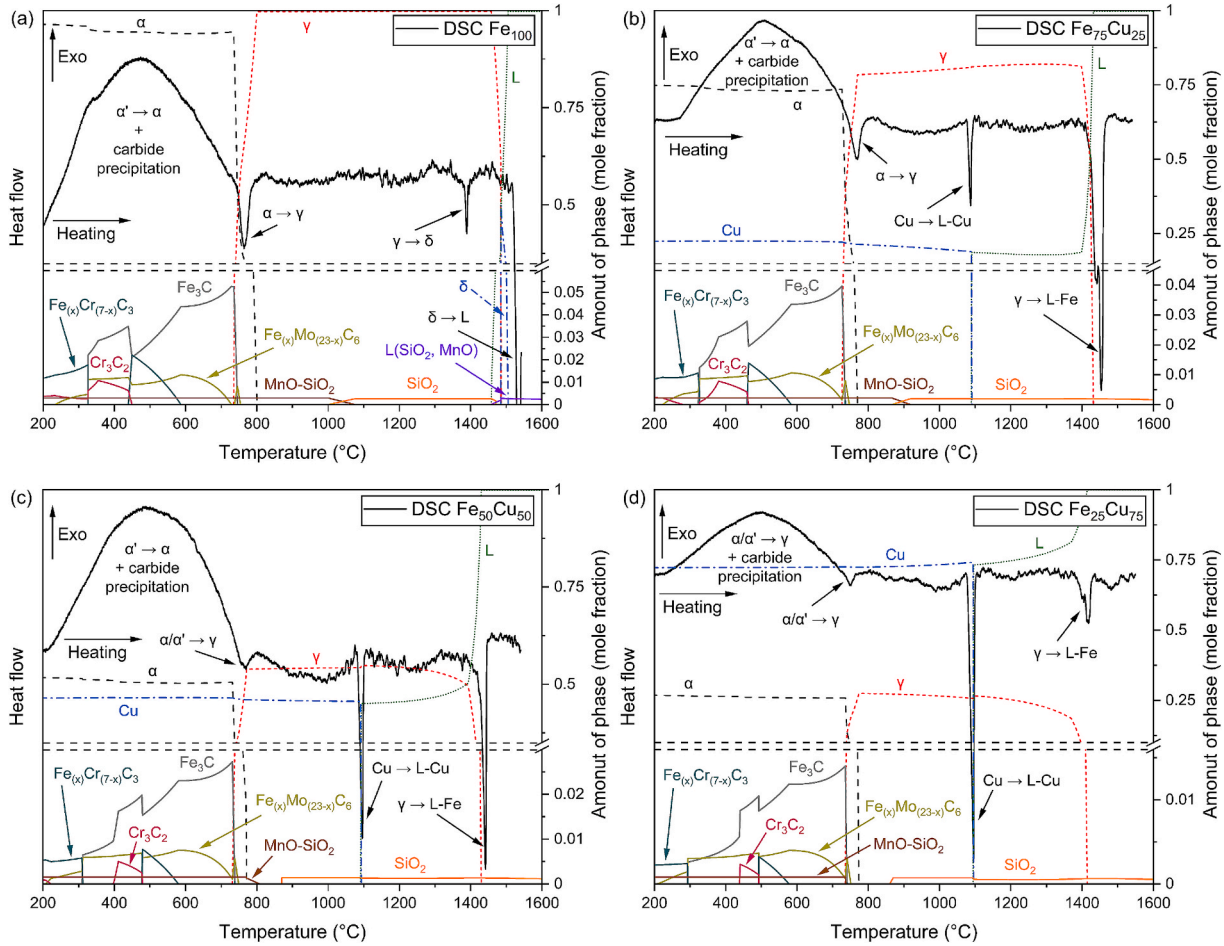

Fig. 9. DSC heating curves and calculated phase transformations of Fe_{100} (a), $Fe_{75}Cu_{25}$ (b), $Fe_{50}Cu_{50}$ (c), and $Fe_{25}Cu_{75}$ (d) blend compositions.

decomposition, expected in the 100–300 °C interval [57], and carbide precipitation occurring over a wider temperature range, as already reported for 4130 steel processed by LPBF [43]. Thermodynamic simulations suggest the formation of various stable carbide phases up to ~750 °C. However, Fe_3C peaks can only be observed in the XRD pattern of Fe_{100} (Fig. 8(b)), while no clear evidence of carbides appears in the diffractograms of the other samples, due to the decreasing intensity of the associated signals as the relative steel content in the blend diminished.

The specimens underwent austenitic transformation (α → γ) and concurrent carbide dissolution above 700 °C. For Fe_{100}, the Ac1 and Ac3 transformation temperatures derived from the onset of the endothermic peak are in good agreement with Thermo-Calc predictions, as shown in Table S2 in the Supplementary Material. The addition of copper to the base steel slightly decreases the predicted transformation temperatures, as Cu acts as a γ stabilizer [58]. However, no significant difference was observed in Ac1 and Ac3 values determined from the experimental curves of Fe_{100} and $Fe_{75}Cu_{25}$, possibly due to the partial overlap between exothermic carbide precipitation and the onset of endothermic α → γ phase transition. Additionally, increasing the Cu from 25 wt% to 75 wt% is not expected to significantly influence the material behavior due to its poor solubility in Fe and the absence of alloying elements in 4130 steel, such as Ni, that could interact with Cu to synergistically promote austenite formation [59]. Copper precipitation from supersaturated steel phases, formed due to rapid solidification during the LDED process [26], was also expected in Cu-containing samples between 600 °C and 800 °C [60]. However, evidence of this phenomenon is not visible in the thermograms, as possible associated peaks are likely masked by carbide precipitation and austenitic transformation occurring in the same temperature range.

The formation of δ-ferrite occurred in Fe_{100} at ~1390 °C, while a prominent peak appeared at ~1540 °C as the sample started melting. In the diagram of Fig. 9(a), the melting peak is partially cut off to make lower intensity peaks more visible in the heat flow curve. Cu-containing samples did not undergo γ → δ transformation at high temperature, since the stability domain of the δ phase in the Fe-Cu diagram is not crossed for Cu contents above ~15 wt% (Fig. 1). For these compositions, a first melting peak can be observed at ~1085 °C, approximately corresponding to the melting point of copper, while a second peak appears above 1400 °C due to melting of the austenite phase. Since the equilibrium calculations could not accurately determine the relative amount of immiscible liquid phases within the metastable miscibility gap of the Fe-Cu system (Fig. 1), a single liquid phase was reported in the diagrams of Fig. 9(b-d) by summing the contributions from both Cu- and Fe-rich liquid phases.

3.3. As-built microstructure

The microstructure of as-built Fe_{100} primarily consists of ferritic domains with polygonal and acicular morphology in melt pool core and boundary regions, respectively, as shown in Fig. 10(a-b). The formation of acicular ferrite at the melt pool boundaries regions has also been observed in ferritic steel parts manufactured by arc-based DED [61] and can be attributed to the steep thermal gradient and directional heat flow toward the underlying solid layers. On the other hand, the slower cooling rate experienced by the inner regions of the melt pools promoted the development of polygonal grains. The tempered martensite and dispersed needle-shaped carbides observed in SEM micrographs at higher magnification (Fig. 10(c)) resulted from an in-situ tempering effect induced by the heat provided during the deposition of subsequent layers. Similar microstructural features have been previously reported for 4130 steel processes by LPBF [43]. EBSD analysis did not reveal any preferential crystallographic orientation that could be linked to the layerwise process (Fig. 10(d)). This may be attributed to γ → α/α' transformation occurring during cooling [62], which rearranges the grains and prevents the development of strong textures typical of parts manufactured by LDED [53]. The phase map in Fig. 10(d) highlights the presence of retained/reversed austenite, as previously indicated by XRD results (Fig. 8(b)), dispersed in a α/α' matrix at a content of ~0.4 %. It should be noted that the austenite content in the bulk material may be significantly higher than that measured through EBSD, as the stress introduced during polishing operations can cause its removal from the surface regions.

As-built $Fe_{75}Cu_{25}$, $Fe_{50}Cu_{50}$, and $Fe_{25}Cu_{75}$ samples exhibited a martensitic microstructure in Fe-rich areas, as shown in Fig. 11. No evident ferrite grains were observed, as the higher cooling rate induced by copper additions to the base steel suppressed ferrite formation and promoted γ → α' transformation during cooling. This is also suggested by the results of EBSD analysis, which reveals a higher fraction of high-angle grain boundaries (HAGBs) in the Fe-rich regions of blend composition samples compared to Fe_{100} (see representative misorientation data in Fig. S2 of the Supplementary Material). Abdelwahed et al. [43] attributed the relatively high fraction of HAGBs measured in 4130 steel processed by LPBF to the fully martensitic microstructure promoted by rapid solidification and cooling.

Copper grains in Cu-rich areas of $Fe_{50}Cu_{50}$ and $Fe_{25}Cu_{75}$ mostly appear as equiaxed, as shown in Fig. 12(a,d). The formation of fine equiaxed grains with random orientation (Fig. 12(b,e)) is promoted by the already solidified Fe particles, which provide numerous sites for heterogeneous nucleation (see Section 6 in the Supplementary Material). In the $Fe_{50}Cu_{50}$ sample, grains in Cu-rich areas exhibit an irregular shape (Fig. 12(b,c)) because their growth is constrained within relatively narrow bands squeezed between the wider Fe-rich regions. In contrast, in the $Fe_{25}Cu_{75}$ sample, grains can develop a more rounded morphology (Fig. 12(e,f)) as they grow in larger areas due to the lower steel content in the blend composition. It can be noticed from Fig. 12(d, e) that the size of copper grains in $Fe_{25}Cu_{75}$ depends on the local density of nucleation sites. In areas with a high concentration of Fe particles and

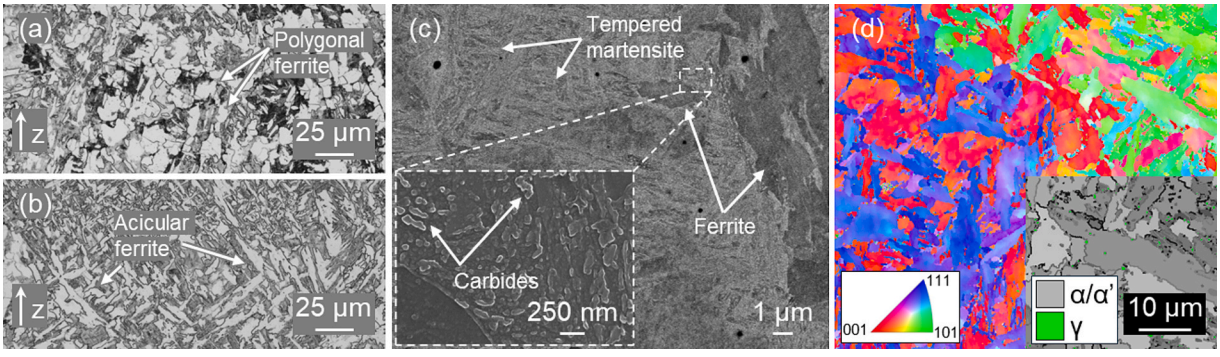

Fig. 10. Ferrite morphology in melt pool core (a) and boundary (b) regions, detail of martensite laths (c), and IPF map of Fe_{100}, with a phase map overlay highlighting the distribution of retained/reversed austenite (d).

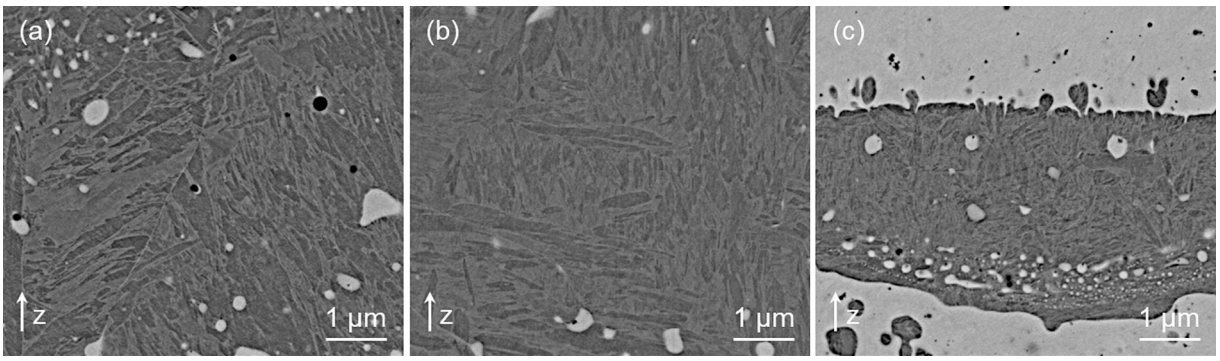

Fig. 11. BSE micrographs showing the martensitic microstructure in Fe-rich regions in $Fe_{75}Cu_{25}$ (a), $Fe_{50}Cu_{50}$ (b), and $Fe_{25}Cu_{75}$ (c). Fe-rich regions appear dark grey, while Cu-rich regions appear light grey.

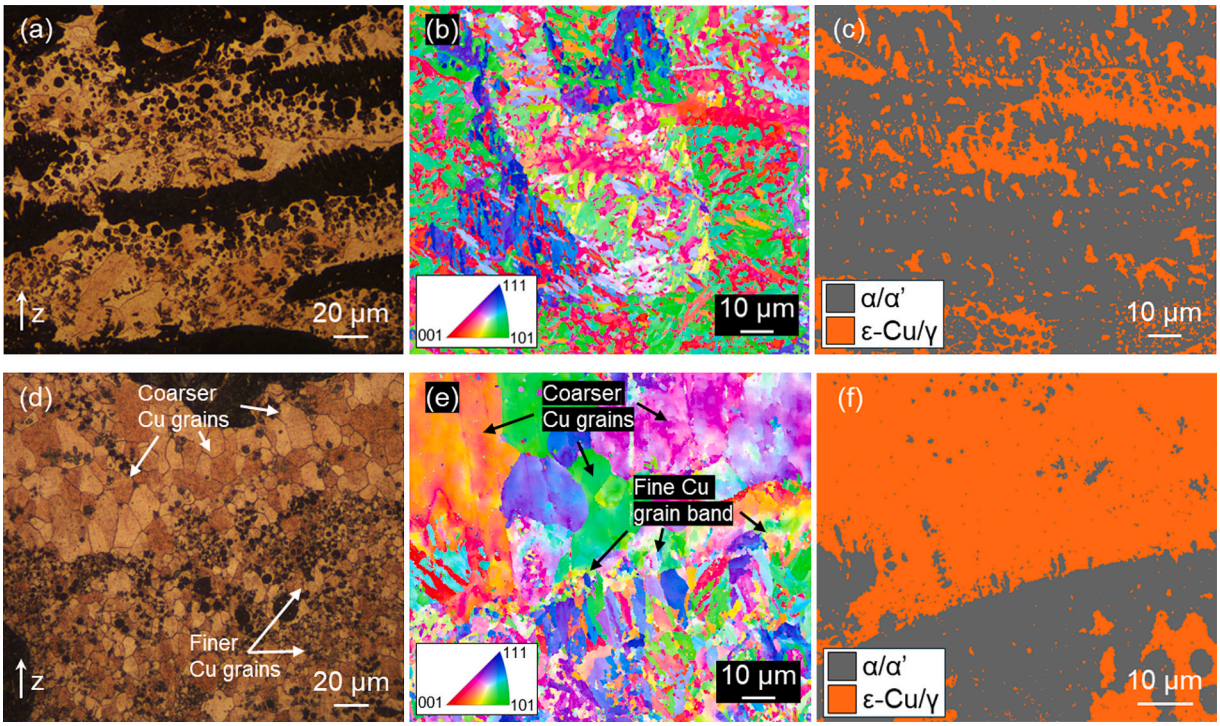

Fig. 12. As-built microstructure in Cu-rich areas and IPF maps with corresponding phase distribution of $Fe_{50}Cu_{50}$ (a-c) and $Fe_{25}Cu_{75}$ (d-f).

at the interface with Fe-rich bands, grains are finer because many nuclei are formed and undergo limited growth. On the other hand, in regions with a lower concentration of Fe particles and farther from Fe-rich bands, fewer nuclei undergo greater growth, leading to the formation of relatively coarser grains. The grain size distribution plots of $Fe_{25}Cu_{75}$ can be found in Fig. S3 of the Supplementary Material.

3.4. Mechanical properties

Fig. 13 shows representative load–displacement plots recorded during the indentation plastometry tests conducted on as-built parts, along with the stress–strain curves calculated from best-fit Voce hardening parameters. Data are reported only for Fe_{100}, $Fe_{50}Cu_{50}$, and $Fe_{25}Cu_{75}$, as reliable measurements could not be performed on the $Fe_{75}Cu_{25}$ sample due to the extensive presence of cracks and large pores. The area under the load–displacement curves was calculated using the integration tool in OriginPro software to evaluate the effect of blend composition on the energy-absorption capacity of the samples. $Fe_{50}Cu_{50}$ exhibits a larger subtended area compared to Fe_{100} (Table 3), indicating an increase in the deformation capability resulting from the formation of Cu-rich ductile bands (Fig. 3(c)), while the alternating Fe-rich bands required a load comparable to Fe_{100} to reach the target plastic strain during the test. On the other hand, although $Fe_{25}Cu_{75}$ was expected to display a high energy-absorption capacity due to its high Cu content, the area under the curve is significantly smaller compared to the other samples due to the relatively low load required to achieve the ultimate plastic strain. However, when comparing only the portion of the curves corresponding to the first loading step, extending up to ~0.4 kN for all samples (see inset of Fig. 13(a)), it can be observed that both the subtended area and the indenter displacement increase with the Cu content. Specifically, the fractional area under the curve is 5.3 ± 0.2 N · mm, 5.7 ± 0.3 N · mm, and 8.2 ± 0.1 N · mm for Fe_{100}, $Fe_{50}Cu_{50}$, and $Fe_{25}Cu_{75}$, respectively. This suggests an increasing deformation capability under relatively low loads, consistent with the findings of Yadav et al. [26] for Cu-304 SS multimaterial parts fabricated by LDED.

The estimated tensile properties and hardness of the as-built samples are summarized in Table 3. As expected, increasing the Cu content in the blend composition results in a gradual reduction in yield strength (YS), as the soft Cu-regions promote the earlier onset of plastic deformation. In contrast, the other mechanical properties display a more complex

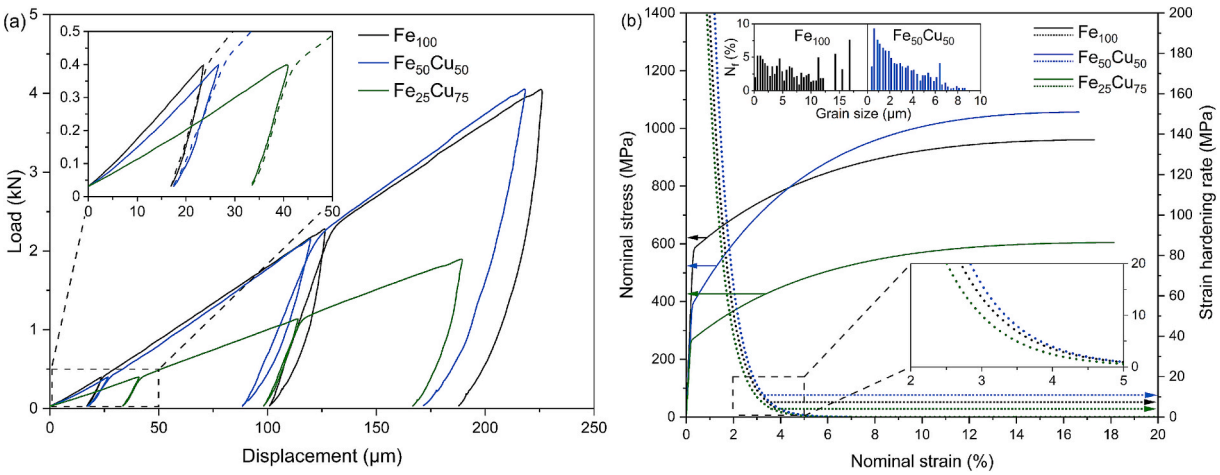

Fig. 13. Representative load–displacement (a) and calculated stress–strain and strain hardening curves (b) of as-built Fe_{100}, $Fe_{50}Cu_{50}$, and $Fe_{25}Cu_{75}$. The grain size distribution of Fe_{100} and $Fe_{50}Cu_{50}$ samples, expressed as number fraction, is also presented in the insets of Fig. 13(b). Experimental data are not reported for $Fe_{75}Cu_{25}$ as reliable measurements could not be performed due to the extensive presence of cracks and large pores.

Table 3
Indentation and hardness data of as-built Fe_{100}, $Fe_{50}Cu_{50}$, and $Fe_{25}Cu_{75}$. Experimental data are not reported for $Fe_{75}Cu_{25}$ as reliable measurements could not be performed due to the extensive presence of cracks and large pores.

Sample	Area under the curve (N · m)	Yield strength (MPa)	Ultimate tensile strength (MPa)	Fracture elongation (%)	Brinell hardness (kg mm^{-2})	Vickers microhardness (HV_1)
Fe_{100}	0.46 ± 0.06	555 ± 23	913 ± 9	17 ± 1	268 ± 12	289.9 ± 13.3
$Fe_{50}Cu_{50}$	0.55 ± 0.01	426 ± 39	1018 ± 20	16 ± 1	261 ± 19	311.3 ± 12.3
$Fe_{25}Cu_{75}$	0.20 ± 0.01	264 ± 20	602 ± 21	18 ± 1	142 ± 4	155.3 ± 14.9

behavior, deviating from a simple linear relationship. Compared to the data reported for 4130 steel processed by LPBF [43], Fe_{100} shows significantly lower ultimate tensile strength (UTS) and microhardness, but nearly three times higher elongation at break. This can be primarily attributed to the different microstructures arising from the distinct cooling rates in the LPBF and LDED processes. In LPBF, the faster cooling promotes the formation of a partially tempered martensitic microstructure [43], which contributes to the high UTS and microhardness. On the other hand, the lower cooling rate of LDED leads to the development of a large fraction of softer ferritic domains (Fig. 10(a-b)), resulting in lower strength properties and enhanced ductility.

The significantly higher UTS and microhardness of $Fe_{50}Cu_{50}$ compared to the base steel can be attributed to several factors. The higher cooling rate induced by the introduction of Cu in the blend composition led to the development of a finer microstructure, which strengthens the material through the Hall-Petch mechanism. This is evidenced by the plots shown in Fig. 13(b), where both Fe_{100} and $Fe_{50}Cu_{50}$ samples exhibit relatively wide grain size distributions with average dimensions of 7 ± 5 μm and 2.9 ± 1.9 μm, respectively. Moreover, the rapid solidification inhibited the formation of ferrite, leading to the prevalence of harder martensitic constituents (Fig. 11(b)), and contributed to solid solution strengthening by inducing the generation of Cu- and Fe-rich phases supersaturated in Fe and Cu, respectively, as demonstrated by EDS measurements. The fine particles formed through secondary liquid phase separation (Fig. 6) provided an additional dispersion hardening effect. Although not directly observable at the magnifications considered in this work, previous studies [26,45] also highlighted the role of nano-sized particles precipitating from supersaturated solid phases in enhancing the mechanical properties of additively manufactured copper-steel multimaterial parts. Compared to Fe_{100}, the increase in UTS in $Fe_{50}Cu_{50}$ is achieved without a significant reduction in the fracture elongation, owing to the presence of Cu-rich bands with good deformability, as discussed in the analysis of load–displacement data. $Fe_{50}Cu_{50}$ also exhibits a higher strain hardening rate θ (Fig. 13), calculated from true stress–strain data using Equation (3).

$$\theta = \frac{\partial \sigma}{\partial \varepsilon} \tag{3}$$

The increased strain hardening rate can be attributed to the interaction between hard α/α' and the soft ε-Cu domains within the material. Local microhardness measurements revealed a significant difference between Fe- and Cu-rich areas in $Fe_{50}Cu_{50}$, displaying microhardness values of 658.6 ± 36.6 $HV_{0.025}$ and 134.6 ± 10.4 $HV_{0.025}$, respectively. These data are not directly comparable with those obtained using a higher test load, as the size of the indentations generated by the small 25 gf load is largely influenced by the elastic recovery that occurs when removing the indenter. However, they provide a useful comparison between the properties of the different regions within the heterogeneous structure. The interaction between hard and soft domains in $Fe_{50}Cu_{50}$ influences the mechanisms of dislocation generation during plastic deformation, as geometrically necessary dislocations (GNDs) originate at the Fe-Cu interfaces to accommodate the strain mismatch between regions with differing plastic behavior [55]. The accumulation of GNDs can increase the flow stress and promote strain hardening. This additional mechanism may have contributed to the improved strength properties of $Fe_{50}Cu_{50}$ and helps explain the comparable Brinell hardness observed in Fe_{100} and $Fe_{50}Cu_{50}$ samples (Table 3), despite the extensive presence of soft Cu-rich areas in the latter. Kernel average misorientation (KAM) maps were constructed from EBSD data to detect a possible increase in local crystal misorientation at the interface between α/α' and ε-Cu phases due to GND accumulation, as shown in Fig. S4 of the Supplementary Material. Although some regions of increased misorientation can be observed near the interfaces, further analysis at higher magnifications is needed to confirm the presence and distribution of GNDs in the material.

The increased Cu content in $Fe_{25}Cu_{75}$ results in significantly lower UTS and hardness and a slightly higher fracture elongation compared to

the other samples (Table 3), because its mechanical behavior is largely dominated by the continuous Cu-rich matrix observed in Fig. 3(d). However, as previously discussed for $Fe_{50}Cu_{50}$, strengthening mechanisms related to fine grain size (Fig. 12(d-e)), martensitic constituents in Fe-rich bands (Fig. 11(c)), finely dispersed particles across supersaturated solid phases (Fig. 7), and the interaction between hard α/α' and the soft ε-Cu domains contribute to maintaining relatively high mechanical properties.

Fig. 14 displays representative micrographs of plastometry indents in the tested specimens. In Fe_{100} and $Fe_{25}Cu_{75}$, the regions around the indents show numerous plastic deformation bands, with no clearly visible cracks (Fig. 14(a,c)). Conversely, the $Fe_{50}Cu_{50}$ sample exhibits numerous cracks originating from the indent and propagating through Cu-rich regions (Fig. 14(b)). Higher magnification SEM and EDS analysis (Fig. 14(d)) revealed that cracking occurred within the Cu-rich bands rather than at the Fe-Cu interface, indicating a strong interfacial bonding between the constituents of the heterogeneous structure in $Fe_{50}Cu_{50}$.

3.5. Thermal characterization

Fig. 15 presents the dilatometry plots of the as-built samples, alongside the calculated linear CTE. The valley observed in the dilatation curves at ~740 °C corresponds to the austenitic transformation. This valley is most prominent in Fe_{100} and its depth progressively diminishes as the Cu content increases in the blend composition samples, because the fraction of α phase undergoing austenitic transformation decreases and the associated volume shrinkage is partially compensated by the thermal expansion of ε-Cu. Ac1 and Ac3 temperatures estimated from the onset of the α → γ valley are consistent with the values determined by Thermo-Calc and DSC calculations (see Table S2 in the Supplementary Material). As discussed earlier, the transition temperatures slightly decrease with the initial addition of copper to the base steel, as Cu is a γ stabilizer [58]. However, further increases in Cu content in $Fe_{50}Cu_{50}$ and $Fe_{25}Cu_{75}$ have no significant impact, as its solubility limit in Fe is already exceeded in $Fe_{75}Cu_{25}$.

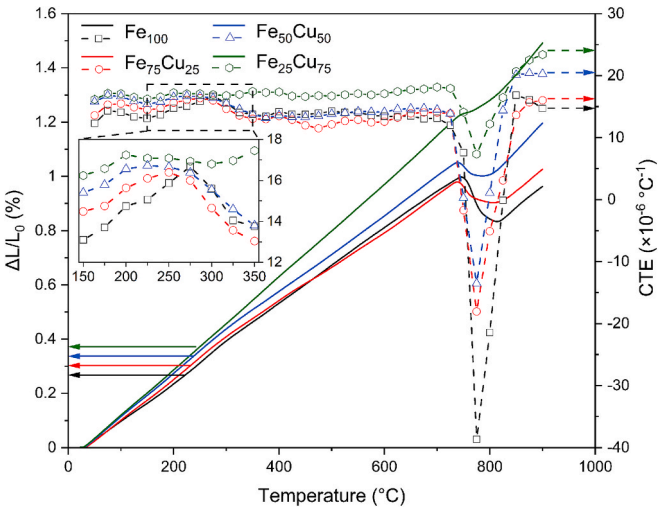

Fig. 15. Dilatometry curves and CTE trends of Fe_{100}, $Fe_{75}Cu_{25}$, $Fe_{50}Cu_{50}$, and $Fe_{25}Cu_{75}$.

The CTEs calculated at room temperature and averaged over the 50–700 °C temperature interval, corresponding to the stability range of the α/α' phase, are in good agreement with the theoretical values derived from literature data using the rule of mixtures [63,64], as shown in Table 4. It can be observed that both the room temperature CTE and the total expansion measured during the dilatometry tests increase with the Cu content, reflecting the higher CTE of copper compared to 4130 steel. However, at higher temperatures $Fe_{75}Cu_{25}$ displays a significantly lower CTE than Fe_{100}. This discrepancy can be attributed to the extensive presence of voids in the specimen due to gas pores and solidification cracks (Fig. 3(b)), which partially offset the thermal expansion of the

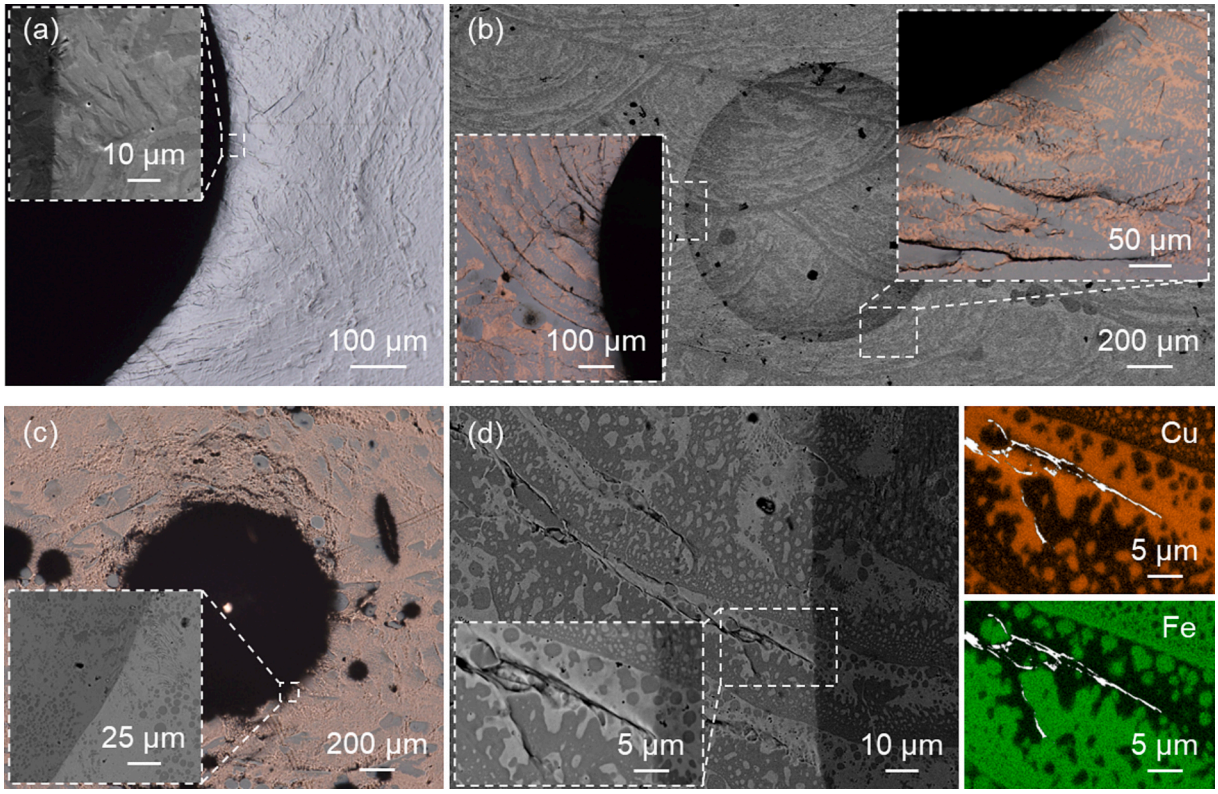

Fig. 14. Plastometry indents in Fe_{100} (a), $Fe_{50}Cu_{50}$ (b), and $Fe_{25}Cu_{75}$ samples (c) and detail of cracked region in $Fe_{50}Cu_{50}$ with corresponding EDS maps (d).

Table 4
Theoretical and experimental CTE calculated at room temperature and in the 50–700 °C range.

Sample	CTE (25 °C, × 10^{-6} °C^{-1})		CTE (50–700 °C, × 10^{-6} °C^{-1})	
	Theor.	Exp.	Theor.	Exp.
Fe_{100}	12.2	12.3	13.2	14.0 ± 0.9
$Fe_{75}Cu_{25}$	13.5	13.6	14.3	13.9 ± 1.3
$Fe_{50}Cu_{50}$	14.8	15.8	15.3	14.9 ± 1.2
$Fe_{25}Cu_{75}$	16.1	16.2	16.4	17.0 ± 0.5

bulk regions, resulting in a lower effective CTE than expected. Notably, the CTEs of all investigated samples display a slight bump peaking at ~275 °C, followed by a decline up to ~350 °C, as evidenced in the inset of Fig. 15. Based on the findings of Matlakhova et al. [57] for 4130 steel in as-quenched condition, this trend can be attributed to the thermal decomposition of martensite, followed by the decomposition of retained/reversed austenite. The non-linearity is evident in the CTE trend of Fe_{100}, $Fe_{75}Cu_{25}$, and $Fe_{50}Cu_{50}$, while it becomes less pronounced in $Fe_{25}Cu_{75}$ because the possible fluctuations associated with the decomposition of small amounts of unstable α' and γ phases are masked by the thermal expansion of the more abundant ε-Cu phase. The apparent negative CTE observed in Fe_{100}, $Fe_{75}Cu_{25}$, and $Fe_{50}Cu_{50}$ between 750 and 800 °C is attributed to the volume contraction caused by the austenitic transformation. The CTE of $Fe_{25}Cu_{75}$ exhibits a slight drop in the same temperature range but remains positive because the shrinkage due to the α → γ phase change is largely compensated by the thermal expansion of the more abundant ε-Cu phase.

Fig. 16(a) shows the thermal diffusivity of the as-built parts, alongside the experimental data of the pure copper reference sample. Compared to the base steel, $Fe_{75}Cu_{25}$ exhibits a lower thermal diffusivity at room temperature and only a modest increase over the temperature range considered, despite the relatively high Cu content in the blend composition. This can be primarily attributed to the microstructural defects observed in $Fe_{75}Cu_{25}$ samples, such as gas pores and solidification cracks, which reduced the effective thermal diffusivity of the material. Additionally, the macrostructure of $Fe_{75}Cu_{25}$ consists of isolated Cu-rich droplets embedded in a continuous Fe-rich matrix (Fig. 3(b)), which governs the thermal behavior of the material, with only a minor contribution from Cu-rich clusters. On the other hand, $Fe_{50}Cu_{50}$ and $Fe_{25}Cu_{75}$ show ~50 % and ~200 % higher thermal diffusivity than Fe_{100}, respectively, corresponding to ~13 % and ~26 % of the pure copper reference. This improvement derived from the formation of interconnected Cu-rich regions in these samples (Fig. 3(c-d)), which

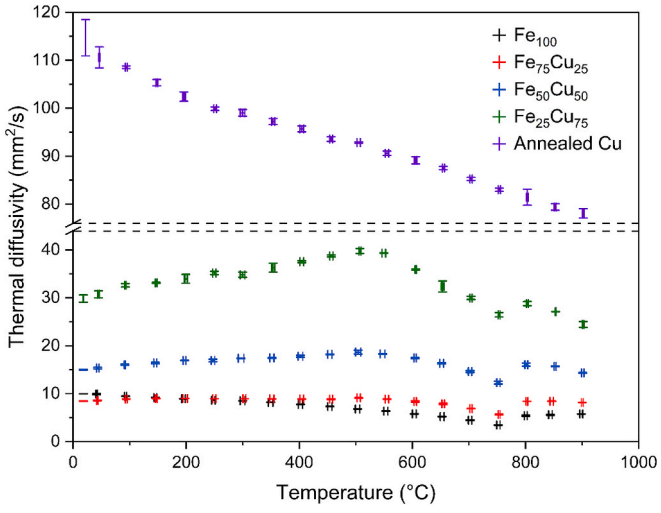

Fig. 16. Thermal diffusivity of Fe_{100}, $Fe_{75}Cu_{25}$, $Fe_{50}Cu_{50}$, and $Fe_{25}Cu_{75}$ compared with pure copper reference sample.

provided a substantial contribution to thermal diffusivity.

It can be observed that the thermal diffusivity of Fe_{100} gradually decreases over the 20–750 °C interval, as previously reported for other low-alloy steel grades [65,66]. This behavior is attributed to the enhanced scattering of free electrons, which govern heat transfer at elevated temperatures, due to stronger lattice vibrations and the higher equilibrium concentration of point defects, such as vacancies and interstitials. In contrast, the thermal diffusivity of $Fe_{75}Cu_{25}$, $Fe_{50}Cu_{50}$, and $Fe_{25}Cu_{75}$ increases with the temperature up to ~500 °C as a result of a tempering effect induced by the thermal cycle applied during the LFA experiments. The relatively high temperature promotes carbide precipitation, as also observed in the DSC measurements (Fig. 9), removing alloying elements such as Cr, Mo, and C from the α solid solution. Since these elements reduce the concentration of free electrons when in solid solution in Fe [65], the formation of precipitates can positively influence the thermal diffusivity. The precipitation of Mo-containing carbides at moderate temperatures (starting at ~200 °C according to Thermo-Calc calculations) may further contribute to thermal diffusivity enhancement by reducing phonon scattering caused by massive Mo atoms occupying substitutional sites in the Fe lattice, as well as by alleviating the strain induced by C atoms in interstitial positions [65]. The phonon contribution to thermal diffusivity may also improve with the reduction of dislocation density during tempering. Unlike the blend composition samples, where Fe-rich regions are fully martensitic (Fig. 11), the thermal diffusivity of Fe_{100} does not appear to benefit from the effects of tempering, probably because its initial microstructure already comprises extensive ferritic domains.

Above ~500 °C, the thermal diffusivity of $Fe_{75}Cu_{25}$, $Fe_{50}Cu_{50}$, and $Fe_{25}Cu_{75}$ starts decreasing due to thermal scattering of free electrons prevailing over possible tempering effects. The trends exhibited by the Fe_{100} and pure copper samples indicate that both Fe- and Cu-rich regions experience a temperature-dependent reduction in thermal diffusivity. This effect is further amplified during the α → γ phase change due to the coexistence of domains with different crystal structures and solubility for alloying elements, which results in the drop observed at ~750 °C, roughly corresponding to the onset of the austenitic transformation (see Table S2 in the Supplementary Material). Once the transition to the austenitic phase is complete at ~800 °C, the microstructural homogeneity results in an initial increase in thermal diffusivity, followed by a gradual reduction at higher temperatures due to more intense electron scattering. A comparison between the thermal diffusivity data collected during the first and second thermal cycles applied in LFA experiments can be found in Fig. S5 of the Supplementary Material.

3.6. Response to heat treatment

Fig. 17 shows representative optical and SEM micrographs of heat-treated Fe_{100} and $Fe_{50}Cu_{50}$ samples taken at different magnifications. It can be observed that the Q + T treatment homogenized the macrostructure of Fe_{100}, with the melt pools characteristic of the as-built state no longer visible (Fig. 17(a)). The microstructure primarily consists of tempered martensite and uniformly distributed ferrite domains with significantly smaller size compared to as-built parts (Fig. 3(a)). Tempering also promoted the precipitation of finely dispersed carbides within the martensite regions, as confirmed by XRD (Fig. 18). Due to the absence of an initial high temperature austenitization step, the original melt pool boundaries are still visible in the Fe_{100} sample following DT treatment, as evidenced in Fig. 17(b). However, the heat-treated material displays a much finer lath-like microstructure compared to the as-built condition. The results of XRD analysis (Fig. 18) indicate that both heat treatments induced the thermal decomposition of retained/reversed austenite, as also suggested by EBSD phase maps revealing an austenite content below the detection limit.

In $Fe_{50}Cu_{50}$ samples, the applied heat treatments did not visibly alter the original macrostructure resulting from the phase separation between immiscible Fe and Cu, as shown in the low magnification optical

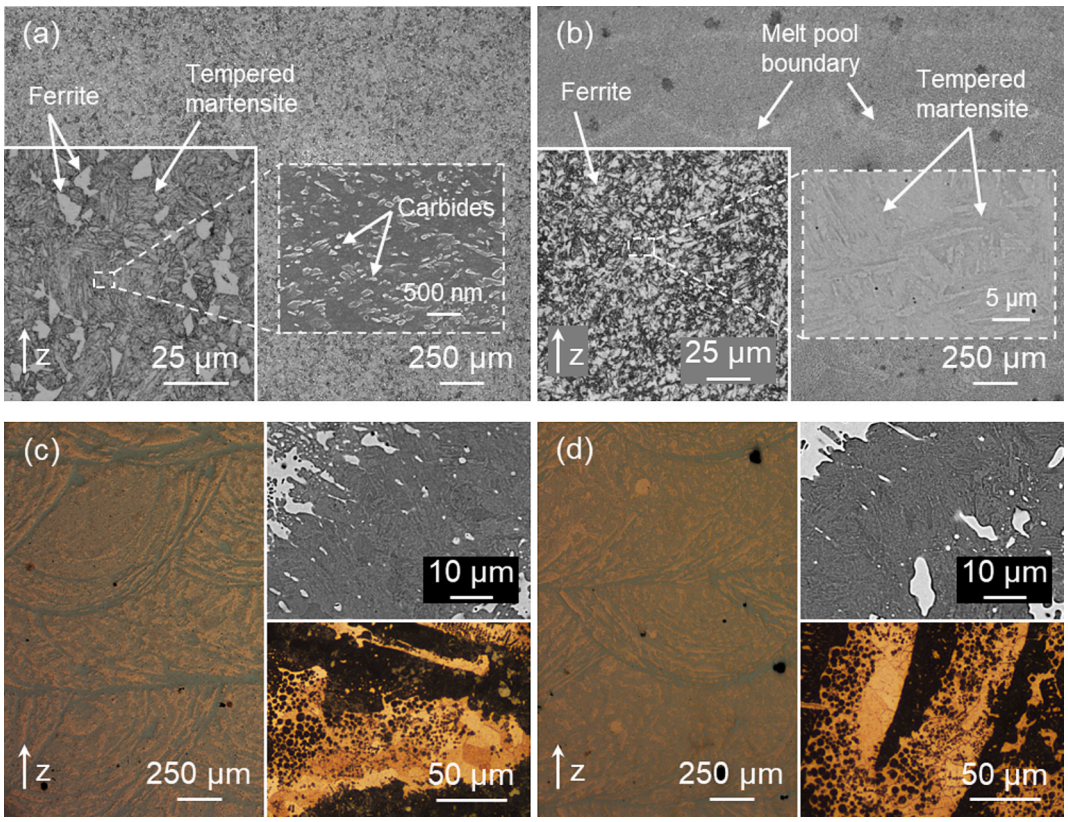

Fig. 17. Macrostructure morphology and microstructure of quenched and tempered (a) and direct tempered Fe_{100} (b), quenched and tempered (c) and direct tempered $Fe_{50}Cu_{50}$ (d).

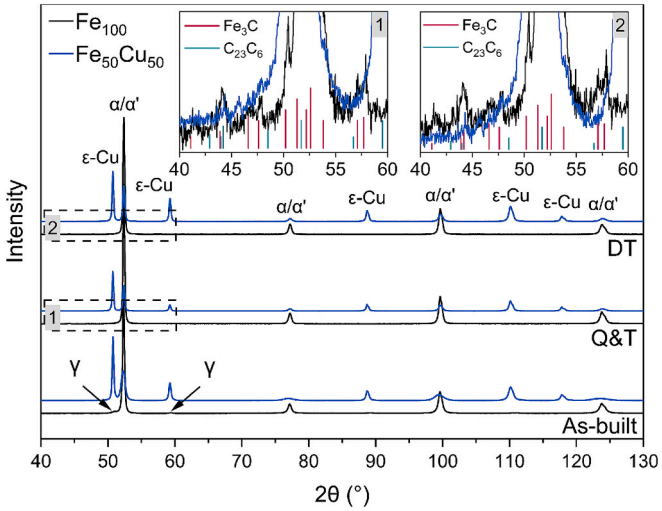

Fig. 18. XRD patterns of Fe_{100} and $Fe_{50}Cu_{50}$ in as-built and heat-treated conditions.

micrographs in Fig. 17(c-d). The microstructure in Fe-rich regions predominantly consists of martensite, while Cu-rich bands exhibit equiaxed grains likely formed by recrystallization, which can be activated already below 300 °C [67]. The diffraction peaks observed in the XRD patterns of heat-treated $Fe_{50}Cu_{50}$ suggest that the same carbide precipitation mechanisms occur during tempering as in the base steel. The analysis of the diffraction peaks reveals a consistent shift of the α/α' peaks toward higher diffraction angles (by 0.1–0.3 °C), with a corresponding slight decrease in the lattice constant, compared to the as-built state. This may indicate a reduced lattice distortion, possibly due to Cu diffusion from the supersaturated Fe-based solid solution during heat treatment. The similarity in diffraction angles and lattice constants between the two heat-treated conditions suggests that diffusion can already occur at the moderate temperature applied during the tempering stage. Regarding the ε-Cu phase, no significant peak shifts are observed between the as-built and heat-treated samples, indicating limited diffusion of elements in solid solution within the Cu-rich phase. This aligns with the results of EDS analysis, which showed a low Fe content in the Cu-rich bands of the as-built material. Additional details on peak shift analysis are provided in Section 7 of the Supplementary Material.

Fig. 19 compares the load–displacement and stress–strain curves of Fe_{100} and $Fe_{50}Cu_{50}$ in as-built and heat-treated conditions. The main plastometry and microhardness data are summarized in Table 5. It can be observed that the maximum displacement of Fe_{100}, as well as the calculated fracture elongation, decreases after both heat treatments. On the other hand, the strength and hardness properties show an increasing trend. These changes reflect the microstructural evolution induced by the applied heat treatments, involving the transition from the relatively large ferritic domains of the as-built material (Fig. 10(a-b)) to the finer martensitic constituents observed in the heat-treated samples (Fig. 17(a-b)). The Q + T treatment has the greatest impact on the mechanical properties of Fe_{100}, due to the formation of fresh martensite upon annealing and water quenching. Conversely, the DT treatment is less effective, as tempering is applied to a material that is already partially tempered and contains a significant fraction of ferrite. The area under the first section of the load–displacement curves, corresponding to a maximum load of ~0.4 kN for all samples (see inset of Fig. 19(a)), follows the same trend, with the Q + T treatment leading to a slightly higher reduction than DT. Specifically, the calculated values are 5.3 ± 0.2 N · mm, 5.1 ± 0.3 N · mm, and 5.2 ± 0.2 N · mm for Fe_{100} in as-built, Q + T, and DT conditions, respectively. On the other hand, the total subtended area is larger for the Q + T condition due to the higher load required to achieve the ultimate plastic strain, while it remains largely

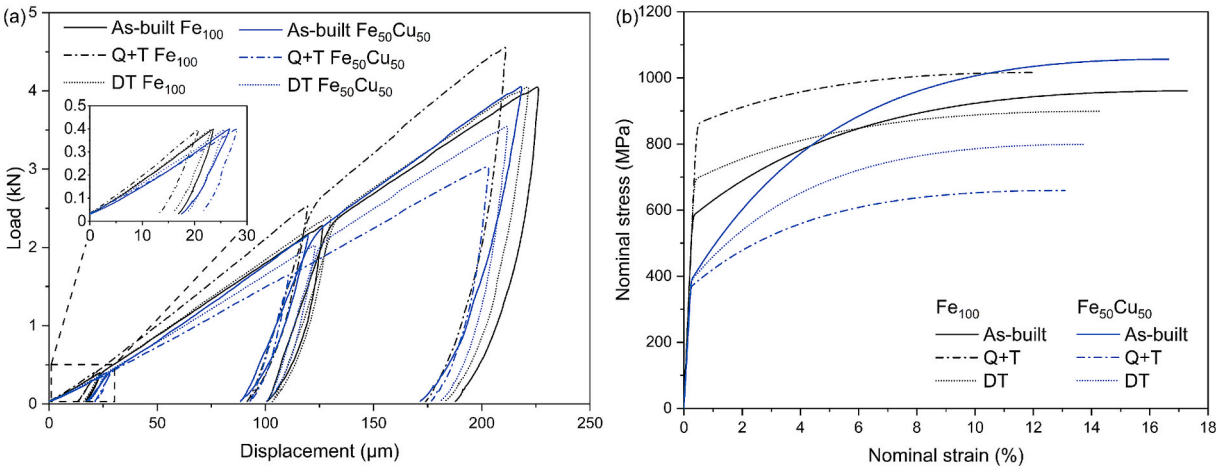

Fig. 19. Representative load–displacement (a) and calculated stress–strain curves (b) of heat-treated Fe_{100} and $Fe_{50}Cu_{50}$.

Table 5
Indentation and hardness data of heat-treated Fe_{100} and $Fe_{50}Cu_{50}$.

Sample	Heat treatment	Area under the curve (N · m)	Yield strength (MPa)	Ultimate tensile strength (MPa)	Fracture elongation (%)	Brinell hardness (kg mm^{-2})	Vickers microhardness (HV_1)
Fe_{100}	Q + T	0.64 ± 0.07	875 ± 18	1002 ± 14	12 ± 1	303 ± 14	329.0 ± 4.8
	DT	0.54 ± 0.01	708 ± 20	900 ± 12	14 ± 1	276 ± 11	295.8 ± 10.7
$Fe_{50}Cu_{50}$	Q + T	0.36 ± 0.02	357 ± 22	666 ± 11	14 ± 2	211 ± 8	216.7 ± 9.9
	DT	0.48 ± 0.03	389 ± 32	782 ± 13	14 ± 1	220 ± 24	222.4 ± 12.5

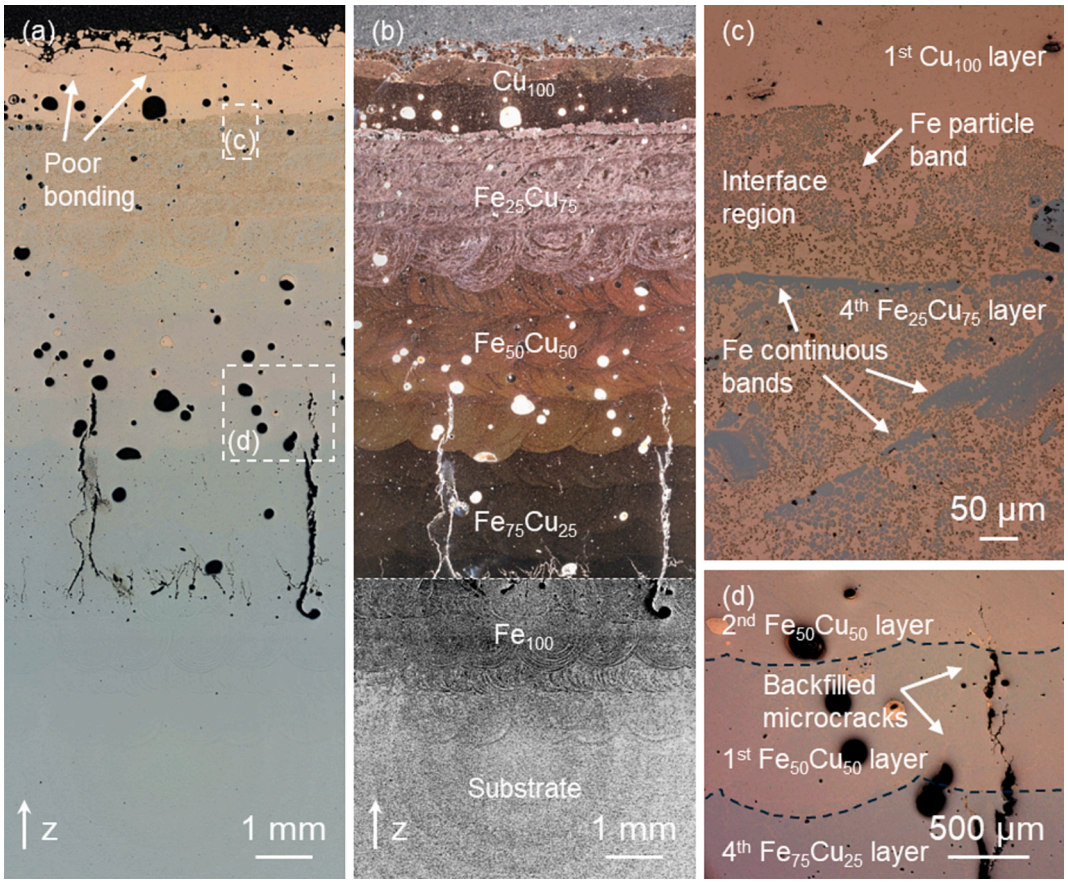

Fig. 20. Cross-sectional view of FGM sample acquired with coaxial lighting (a) and a combination of ring and coaxial lighting (b), interface region between $Fe_{25}Cu_{75}$ and Cu_{100} (c), and solidification cracks in $Fe_{75}Cu_{25}$ and $Fe_{50}Cu_{50}$ layers. The lower portion of Fig. 20(b) is shown with enhanced contrast to highlight the melt pool structure in the Fe_{100} region.

unchanged with the DT treatment compared to the as-built material.

Both heat-treated $Fe_{50}Cu_{50}$ samples display a reduction in strength and hardness properties compared to the as-built condition. The first section of the load–displacement curves shows a slight increase in the indenter displacement and in the subtended area compared to the as-built condition, indicating a higher energy-absorption capacity at low load levels. However, when considering the entire range, the total area decreases significantly due to the diminished load-bearing capacity of the heat-treated parts. This softening effect can be primarily attributed to the recrystallization of copper regions and the diffusion of Cu from supersaturated Fe-rich regions, as suggested by XRD analysis, reducing the contribution of solid solution strengthening mechanism. This is further evidenced by the reduction in local microhardness values measured in Cu-rich regions (96.0 ± 7.3 $HV_{0.025}$ and 122.8 ± 10.9 $HV_{0.025}$ for Q + T and DT conditions, respectively) and Fe-rich rich regions (413.9 ± 10.6 $HV_{0.025}$ and 482.8 ± 21.3 $HV_{0.025}$ for Q + T and DT conditions, respectively) compared to as-built $Fe_{50}Cu_{50}$. Studies on Cu-based systems microalloyed with Fe and Ti reported a predominant hardening effect after solution and aging treatments involving thermal cycles comparable to those applied in the present work, which was primarily attributed to the precipitation of Fe-Ti nanoparticles [68,69]. In contrast, the absence of alloying elements that can readily form nanoprecipitates with Fe in $Fe_{50}Cu_{50}$ may explain its tendency to soften upon tempering. Notably, the more prolonged exposure to higher temperatures in Q + T treatment increased this softening effect compared to DT, indicating a diametrically opposed response of $Fe_{50}Cu_{50}$ to heat treatment compared to Fe_{100}.

3.7. FGM sample characterization

Fig. 20(a-b) shows a cross-sectional view of the FGM sample, with the indication of the constitutive layers. Large macrocracks can be observed originating from the upper Fe_{100} layer and running through the entire $Fe_{75}Cu_{25}$ region, as also found in the corresponding individual blend composition sample (Fig. 3(b)). Solidification cracking in this region can be attributed to thermal stresses developed during the deposition process, due to the mismatch in the thermophysical properties between layers with different chemical composition, as demonstrated by dilatometry (Fig. 15) and LFA measurements (Fig. 16), and to the scarce terminal liquid in $Fe_{75}Cu_{25}$ at the end of solidification. Interestingly, cracks extend into the lower $Fe_{50}Cu_{50}$ layer, where copper veins can completely fill only the thinner microcracks (Fig. 20(d)), although the analysis of the individual blend composition sample did not indicate a significant cracking susceptibility at this nominal composition. A possible explanation is the local reduction in Cu content resulting from the partial remelting of the underlying $Fe_{75}Cu_{25}$ layer during the deposition of the first $Fe_{50}Cu_{50}$ layer, along with the mixing inside the melt pool promoted by Marangoni convention and buoyancy effects, which pull Fe towards the upper regions due to its lower density compared to Cu [17]. Consequently, the material may have been locally depleted in Cu and enriched in Fe compared to its nominal composition, possibly entering the range of susceptibility to solidification cracking. This is also suggested by the results of EDS area measurements taken at different heights of the FGM sample (Fig. 21(a)), which indicate that the Fe and Cu contents vary gradually at the interface between the $Fe_{75}Cu_{25}$ and $Fe_{50}Cu_{50}$ regions rather than undergoing an abrupt change. In fact, the compositional profile of the multilayer structure aligns more closely with the continuous theoretical trend (dash-dot line in Fig. 21(a)), which was calculated assuming that the Fe and Cu contents vary linearly and the nominal composition of each region is reached at its center position, compared to the discrete trend assuming no interlayer dilution (dashed line). The dilution effect diminishes starting from the second $Fe_{50}Cu_{50}$ layer, and no further cracking is observed in the remaining part of the sample. The interface between $Fe_{25}Cu_{75}$ and Cu_{100} consists of a band of Fe-rich particles embedded in a Cu-rich continuous matrix, while the Fe-rich bands observed in the underneath layers disappear, as highlighted in Fig. 21(c). The development of this band can also be attributed to the partial remelting of the upper $Fe_{25}Cu_{75}$ layer during the deposition of the first copper layer, leading to the formation of spherical Fe-rich particles that minimize the surface contact area between the immiscible phases.

Prominent round pores can be observed across the FGM sample, mainly concentrated in the interlayer regions. As discussed for the individual blend composition samples, this porosity likely results from gas entrapment during the LDED process or from Cu boiling due to excessive laser power input. These defects could be mitigated through the optimization of the processing parameters, particularly by adjusting the laser power for each layer based on its chemical composition. Evidence of poor interfacial adhesion between the two Cu_{100} layers can also be seen in Fig. 20(a), attributable to the low energy absorbed during the deposition of the second layer, caused by laser reflection and rapid heat dissipation from the underlying consolidated copper layer.

The microhardness profile measured along the compositional gradient in the FGM sample (Fig. 21(b)) shows an initial increase from the 316 stainless steel substrate (~175 HV_1) to the Fe_{100} region (~512 HV_1), followed by a gradual decreasing trend as the Cu content in the material increases. Wide fluctuations in the measured values can be observed for the $Fe_{50}Cu_{50}$ region, due to the coexistence of randomly distributed hard Fe-rich and soft Cu-rich areas, as also observed by Yadav et al. [26] in Cu-304L FGM parts manufactured by LDED. The $Fe_{75}Cu_{25}$ and $Fe_{25}Cu_{75}$ regions, on the other hand, display smaller deviations because their local mechanical behavior is primarily governed

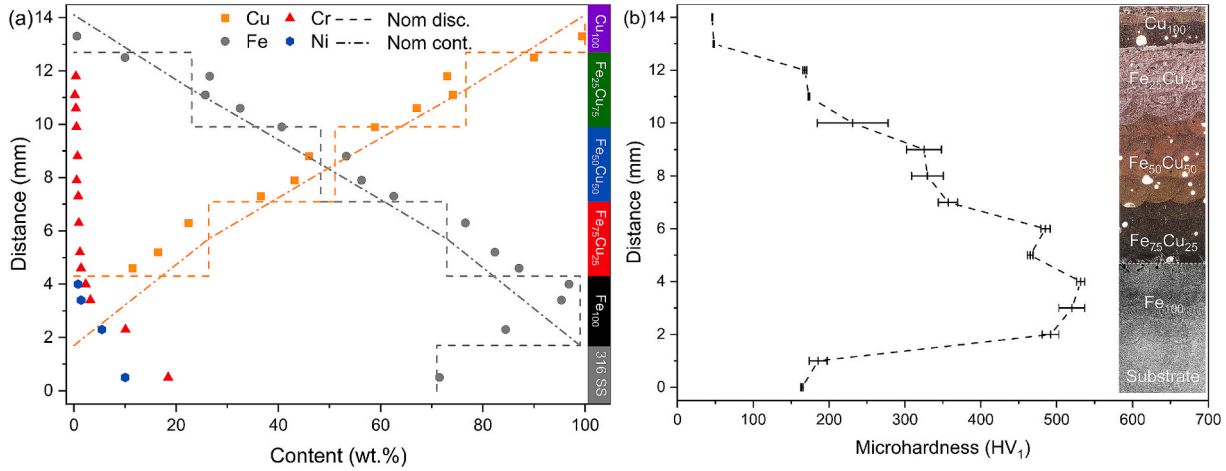

Fig. 21. Chemical composition (a) and microhardness profile (b) measured along the compositional gradient.

by the predominant Fe- and Cu-rich phases, respectively.

4. Conclusions

The present study explored the microstructural, mechanical, and thermophysical properties of the constitutive layers of a functionally graded material fabricated via laser directed energy deposition through in-situ alloying of pure copper and AISI 4130 low-alloy steel powders. Four distinct compositions with varying 4130 and Cu contents were examined in both as-built and heat-treated conditions: 100 % 4130 (Fe_{100}), 75 % 4130 – 25 % Cu ($Fe_{75}Cu_{25}$), 50 % 4130 – 50 % Cu ($Fe_{50}Cu_{50}$), and 25 % 4130 – 75 % Cu ($Fe_{25}Cu_{75}$). A functionally graded material sample was then fabricated by sequentially depositing the investigated blend compositions, followed by pure copper layers. The main outcomes are summarized as follows.

(1) Peculiar macrostructure morphologies resulted from Fe-Cu liquid phase separation and Marangoni convection. $Fe_{75}Cu_{25}$ displayed copper fiber fragments embedded in a Fe-rich matrix, while $Fe_{50}Cu_{50}$ exhibited a recursive macrostructure with copper and steel alternating as matrix and dispersed phase. $Fe_{25}Cu_{75}$ comprised a continuous Cu-rich matrix with Fe-rich regions with globular, dendritic, or blocky shape depending on the local cooling conditions within the melt pool. The chemical composition of printed parts measured by X-ray fluorescence was in good agreement with nominal values.

(2) Thermal stress and insufficient liquid replenishment caused solidification cracking in $Fe_{25}Cu_{75}$, while the abundant Cu-rich terminal liquid in $Fe_{50}Cu_{50}$ backfilled the microcracks formed during the early stages of solidification, leading to defect-free deposits.

(3) The as-built microstructure of Fe_{100} primarily consisted of polygonal/acicular ferrite, tempered martensite with dispersed carbides, and ~0.4 % retained/reversed austenite. The higher cooling rate in blend composition samples suppressed ferrite formation and resulted in a fully martensitic microstructure in Fe-rich regions. Cu-rich areas in $Fe_{50}Cu_{50}$ and $Fe_{25}Cu_{75}$ comprised fine equiaxed grains with random orientation due to Fe-rich domains acting as heterogeneous nucleation sites.

(4) Compared to the base steel, $Fe_{50}Cu_{50}$ exhibited significantly higher strength and hardness and a comparable ductility, attributed to the finer microstructure, martensite constituents in Fe-rich regions, solid solution and dispersion strengthening, and the interaction between hard Fe-rich and soft Cu-rich domains. $Fe_{25}Cu_{75}$ retained considerable mechanical properties through the same mechanisms, although its behavior was dominated by the continuous Cu-rich matrix.

(5) The formation of interconnected Cu-rich regions in $Fe_{50}Cu_{50}$ and $Fe_{25}Cu_{75}$ improved thermal diffusivity by ~50 % and ~200 %, respectively, compared to Fe_{100}, reaching ~13 % and ~26 % the thermal diffusivity of pure copper. Microstructural defects and isolated copper clusters in $Fe_{75}Cu_{25}$ limited its thermal performance despite the relatively high Cu content. The thermal diffusivity of blend composition samples increased up to ~500 °C due to tempering effects increasing free electron concentration and reducing phonon scattering. However, it declined at higher temperatures due to increased electron scattering, with a notable drop at ~750 °C corresponding to the austenitic phase transformation.

(6) Quenching and tempering significantly improved the strength and hardness of Fe_{100} by transforming the relatively large ferritic grains into finer tempered martensitic constituents. Direct tempering had a moderate effect, due to the presence of ferrite and partially tempered martensite in as-built Fe_{100}, which limited the extent of further hardening during additional tempering. On the other hand, both heat treatments led to softening of $Fe_{50}Cu_{50}$ due to copper recrystallization and reduced solid solution strengthening caused by Cu diffusion from supersaturated Fe-rich regions.

(7) In the functionally graded material sample, local deviations from the nominal chemical composition caused by partial remelting of the underlying material during subsequent layer deposition and convection flows in the melt pool extended the zone susceptible to solidification cracking up to the first $Fe_{50}Cu_{50}$ layer. The upper copper layers exhibited poor interfacial adhesion due to laser reflection and rapid heat dissipation, resulting in low effective energy input. The microhardness profile showed a decreasing trend with increasing Cu content, with large deviations in the $Fe_{50}Cu_{50}$ region due to the coexistence of hard Fe-rich and soft Cu-rich domains.

Based on these findings, future work will focus on the optimization of processing parameters and the design of functionally graded structures that prevent the formation of local compositions susceptible to solidification cracking. One potential strategy could involve the adjustment of the laser power input during the deposition process in response to the changing chemical composition across layers. Further analysis of the global mechanical and thermophysical properties of multilayer samples will also complement the insights into local behavior, enabling accurate predictions of their performance in practical applications. Additionally, tailored heat treatment strategies could be explored to leverage the higher thermal diffusivity and potentially enhanced hardenability resulting from copper island and interconnected regions embedded within the steel matrix in Cu-containing layers, aiming to optimize the microstructure and improve the mechanical performance of multi-material parts combining pure copper with low-alloy steels.

CRediT authorship contribution statement

Tobia Romano: Writing – review & editing, Writing – original draft, Methodology, Investigation, Data curation. **Marawan Abdelwahed:** Writing – review & editing, Resources, Investigation, Funding acquisition, Conceptualization. **Virgínia Bertolo:** Writing – review & editing, Software, Investigation. **Tommaso Cecotti:** Investigation, Data curation. **Samuel Skhosane:** Resources, Investigation. **Gautham Mahadevan:** Writing – review & editing, Software, Investigation. **Vera Popovich:** Writing – review & editing, Validation, Supervision, Resources, Funding acquisition. **Marcel Hermans:** Validation, Supervision, Resources, Funding acquisition. **Mohamed A. Taha:** Supervision, Project administration. **Sisa Pityana:** Supervision, Resources, Project administration, Funding acquisition. **Maurizio Vedani:** Writing – review & editing, Validation, Supervision, Resources, Project administration, Funding acquisition, Conceptualization.

Declaration of competing interest

The authors declare that they have no known competing financial interests or personal relationships that could have appeared to influence the work reported in this paper.

Acknowledgements

Dr. Richard Huizenga and Dr. Ruud Hendrikx at the Department of Materials Science and Engineering of the Delft University of Technology are acknowledged for X-ray analyses.

Appendix A. Supplementary data

Supplementary data to this article can be found online at https://doi.org/10.1016/j.matdes.2025.114329.

Data availability

Data will be made available on request.

References

[1] A. Bandyopadhyay, Y. Zhang, B. Onuike, Additive manufacturing of bimetallic structures, Virtual Phys. Prototyp. 17 (2022) 256–294, https://doi.org/10.1080/17452759.2022.2040738.

[2] W. Zhang, H. Liao, Z. Hu, S. Zhang, B. Chen, H. Yang, Y. Wang, H. Zhu, Interfacial characteristics and mechanical properties of additive manufacturing martensite stainless steel on the Cu-Cr alloy substrate by directed energy deposition, J. Mater. Sci. Technol. 90 (2021) 121–132, https://doi.org/10.1016/j.jmst.2021.03.008.

[3] Z.H. Liu, D.Q. Zhang, S.L. Sing, C.K. Chua, L.E. Loh, Interfacial characterization of SLM parts in multi-material processing: metallurgical diffusion between 316L stainless steel and C18400 copper alloy, Mater Charact 94 (2014) 116–125, https://doi.org/10.1016/j.matchar.2014.05.001.

[4] B. Li, C. Han, C.W.J. Lim, K. Zhou, Interface formation and deformation behaviors of an additively manufactured nickel-aluminum-bronze/15-5 PH multimaterial via laser-powder directed energy deposition, Mater. Sci. Eng. A 829 (2022) 142101, https://doi.org/10.1016/j.msea.2021.142101.

[5] G. Phanikumar, S. Manjini, P. Dutta, J. Mazumder, K. Chattopadhyay, Characterization of a continuous CO2 laser-welded Fe-Cu dissimilar couple, Metall. Mater. Trans. A Phys. Metall. Mater. Sci. 36 (2005) 2137–2147, https://doi.org/10.1007/s11661-005-0334-6.

[6] J. Kar, S.K. Roy, G.G. Roy, Effect of beam oscillation on electron beam welding of copper with AISI-304 stainless steel, J. Mater. Process. Technol. 233 (2016) 174–185, https://doi.org/10.1016/j.jmatprotec.2016.03.001.

[7] Y. Poo-arporn, S. Duangnil, D. Bamrungkoh, P. Klangkaew, C. Huasranoi, P. Pruekthaisong, S. Boonsuya, J. Chaiprapa, A. Ruangvittayanon, C. Saisombat, Gas tungsten arc welding of copper to stainless steel for ultra-high vacuum applications, J. Mater. Process. Technol. 277 (2020) 116490, https://doi.org/10.1016/j.jmatprotec.2019.116490.

[8] S. Sebastian, V.A. Suyamburajan, Microstructural analysis of diffusion bonding on copper stainless steel, Mater. Today Proc. 37 (2020) 1706–1712, https://doi.org/10.1016/j.matpr.2020.07.244.

[9] V. Mangla, J.D. Sharma, S. Kumar, P.D. Kumar, A. Agarwal, Joining of stainless steel (SS304) and OFE copper by vacuum brazing, Mater. Today Proc. 26 (2019) 724–727, https://doi.org/10.1016/j.matpr.2020.01.016.

[10] C.F. Tey, X. Tan, S.L. Sing, W.Y. Yeong, Additive manufacturing of multiple materials by selective laser melting: Ti-alloy to stainless steel via a Cu-alloy interlayer, Addit. Manuf. 31 (2020) 100970, https://doi.org/10.1016/j.addma.2019.100970.

[11] C. Pascal, J.M. Chaix, A. Dutt, S. Lay, C.H. Allibert, Elaboration of (Steel/Cemented Carbide) Multimaterial by Powder Metallurgy, Mater. Sci. Forum 534–536 (2007) 1529–1532, https://doi.org/10.4028/www.scientific.net/msf.534-536.1529.

[12] C.P. Martendal, P.D.B. Esteves, L. Deillon, F. Malamud, A.M. Jamili, J.F. Löffler, M. Bambach, Effects of beam shaping on copper-steel interfaces in multi-material laser beam powder bed fusion, J. Mater. Process. Technol. 327 (2024) 118344, https://doi.org/10.1016/j.jmatprotec.2024.118344.

[13] C. Rock, P. Tarafder, L. Ives, T. Horn, Characterization of copper & stainless steel interface produced by electron beam powder bed fusion, Mater. Des. 212 (2021) 110278, https://doi.org/10.1016/j.matdes.2021.110278.

[14] S. Yadav, C.P. Paul, A.K. Rai, A.N. Jinoop, S.S. Kausal, S.K. Dixit, Assessing crack susceptibility in blended copper-stainless steel compositions during laser directed energy deposition-based additive manufacturing, Sci. Technol. Weld. Join. 29 (2024) 134–142, https://doi.org/10.1177/13621718241246352.

[15] G. Chen, X. Shu, J. Liu, B. Zhang, J. Feng, Crystallographic texture and mechanical properties by electron beam freeform fabrication of copper/steel gradient composite materials, Vacuum 171 (2020) 109009, https://doi.org/10.1016/j.vacuum.2019.109009.

[16] M.M. El-Husseiny, A.A. Baraka, O. Oraby, E.A. El-Danaf, H.G. Salem, Fabrication of bimetallic high-strength low-alloy steel/Si-bronze functionally graded materials using wire arc additive manufacturing, J. Manuf. Mater. Process. 7 (2023) 138, https://doi.org/10.3390/jmmp7040138.

[17] L. Liu, D. Wang, G. Deng, C. Han, Y. Yang, J. Chen, X. Chen, Y. Liu, Y. Bai, Laser additive manufacturing of a 316L/CuSn10 multimaterial coaxial nozzle to alleviate spattering adhesion and burning effect in directed energy deposition, J. Manuf. Process. 82 (2022) 51–63, https://doi.org/10.1016/j.jmapro.2022.07.038.

[18] O.M. Al-Jamal, S. Hinduja, L. Li, Characteristics of the bond in Cu-H13 tool steel parts fabricated using SLM, CIRP Ann. - Manuf. Technol. 57 (2008) 239–242, https://doi.org/10.1016/j.cirp.2008.03.010.

[19] C. Wei, Z. Sun, Q. Chen, Z. Liu, L. Li, Additive Manufacturing of horizontal and 3D functionally graded 316L/Cu10Sn components via multiple material selective laser melting, J. Manuf. Sci. Eng. Trans. ASME 141 (2019) 1–8, https://doi.org/10.1115/1.4043983.

[20] L. Liu, D. Wang, C. Han, Y. Li, T. Wang, Y. Wei, W. Zhou, M. Yan, Y. Liu, S. Wei, Y. Yang, Additive manufacturing of multi-materials with interfacial component gradient by in-situ powder mixing and laser powder bed fusion, J. Alloys Compd. 978 (2024) 173508, https://doi.org/10.1016/j.jallcom.2024.173508.

[21] D. Wang, L. Liu, G. Deng, C. Deng, Y. Bai, Y. Yang, W. Wu, J. Chen, Y. Liu, Y. Wang, X. Lin, C. Han, Recent progress on additive manufacturing of multi-material structures with laser powder bed fusion, Virtual Phys. Prototyp. 17 (2022) 329–365, https://doi.org/10.1080/17452759.2022.2028343.

[22] A. Bandyopadhyay, B. Heer, Additive manufacturing of multi-material structures, Mater. Sci. Eng. R Reports 129 (2018) 1–16, https://doi.org/10.1016/J.MSER.2018.04.001.

[23] X. Zhang, C. Sun, T. Pan, A. Flood, Y. Zhang, L. Li, F. Liou, Additive manufacturing of copper – H13 tool steel bi-metallic structures via Ni-based multi-interlayer, Addit. Manuf. 36 (2020) 101474, https://doi.org/10.1016/j.addma.2020.101474.

[24] L. Liu, D. Wang, G. Deng, Y. Yang, J. Chen, J. Tang, Y. Wang, Y. Liu, X. Yang, Y. Zhang, Interfacial characteristics and formation mechanisms of copper–steel multimaterial structures fabricated via laser powder bed fusion using different building strategies, Chinese J. Mech. Eng. Addit. Manuf. Front. 1 (2022) 100045, https://doi.org/10.1016/j.cjmeam.2022.100045.

[25] F.F. Noecker, J.N. DuPont, Functionally graded copper - steel using laser engineered net shaping ™ process, Congr. Proc. ICALEO 2002 – 21st Int. Congr. Appl. Laser Electro-Optics, (2002) 185430. doi: 10.2351/1.5066217.

[26] S. Yadav, C.P. Paul, A.K. Rai, R. Singh, S.K. Dixit, Elucidating laser directed energy deposition based additive manufacturing of copper-stainless steel functionally graded material: Processing and material behavior, J. Manuf. Process. 92 (2023) 107–123, https://doi.org/10.1016/j.jmapro.2023.02.041.

[27] U. Articek, M. Milfelner, I. Anzel, Synthesis of functionally graded material H13/Cu by LENS technology, Adv. Prod. Eng. Manag. 8 (2013) 169–176, https://doi.org/10.14743/apem2013.3.164.

[28] S. Wang, C. Chen, J. Ju, J. Zhou, F. Xue, Suppression of LME cracks in Sn bronze-steel system based on multi-material additive manufacturing, Mater. Lett. 335 (2023) 133775, https://doi.org/10.1016/j.matlet.2022.133775.

[29] M. Zhang, Y. Zhang, M. Du, S. Zhang, L. Lei, Experimental characterization and microstructural evaluation of silicon bronze-alloy steel bimetallic structures by additive manufacturing, Metall. Mater. Trans. A Phys. Metall. Mater. Sci. 52 (2021) 4664–4674, https://doi.org/10.1007/s11661-021-06418-y.

[30] X. Zhang, T. Pan, Y. Chen, L. Li, Y. Zhang, F. Liou, Additive manufacturing of copper-stainless steel hybrid components using laser-aided directed energy deposition, J. Mater. Sci. Technol. 80 (2021) 100–116, https://doi.org/10.1016/j.jmst.2020.11.048.

[31] X. Zhang, L. Li, F. Liou, Additive manufacturing of stainless steel – copper functionally graded materials via Inconel 718 interlayer, J. Mater. Res. Technol. 15 (2021) 2045–2058, https://doi.org/10.1016/j.jmrt.2021.09.027.

[32] A. Chatterjee, E. Sprague, J. Mazumder, A. Misra, Hierarchical microstructures and deformation behavior of laser direct-metal-deposited Cu–Fe alloys, Mater. Sci. Eng. A 802 (2021) 140659, https://doi.org/10.1016/j.msea.2020.140659.

[33] R. Kremer, J. Etzkorn, H. Palkowski, F. Foadian, Corrosion resistance of 316L/CuSn10 Multi-material manufactured by powder bed fusion, Mater 15 (2022) 8373, https://doi.org/10.3390/ma15238373.

[34] E. Uhlmann, Y. Saber, Mechanical properties of steel–copper multi-material samples built by laser powder bed fusion using a graded energy input, Prog. Addit. Manuf. 10 (2024) 475–489, https://doi.org/10.1007/s40964-024-00636-7.

[35] M.K. Imran, S.H. Masood, M. Brandt, S. Bhattacharya, J. Mazumder, Direct metal deposition (DMD) of H13 tool steel on copper alloy substrate: evaluation of mechanical properties, Mater. Sci. Eng. A 528 (2011) 3342–3349, https://doi.org/10.1016/j.msea.2010.12.099.

[36] H. Okamoto, Cr-Cu (Chromium-Copper), J. Phase Equilibria Diffus. 33 (2012) 342–343, https://doi.org/10.1007/s11669-012-0050-z.

[37] J. Miettinen, V.-V. Visuri, T. Fabritius, Carbon-containing thermodynamic descriptions of the Fe–Cr–Cu–Mo–Ni–C system for modeling the solidification of steels, Acta Univ. Ouluensis C 787 (2021).

[38] K. Uruga, K. Sawada, Y. Enokida, I. Yamamoto, Liquid metal extraction for removal of molybdenum from molten glass containing simulated nuclear waste elements, J. Nucl. Sci. Technol. 45 (2008) 1063–1071, https://doi.org/10.1080/18811248.2008.9711893.

[39] M.A. Turchanin, P.G. Agraval, A.R. Abdulov, Phase equilibria and thermodynamics of binary copper systems with 3d-metals. IV. Copper-manganese system, Powder Metall. Met. Ceram. 45 (2006) 569–581, https://doi.org/10.1007/s11106-006-0121-y.

[40] H. Okamoto, Cu-Si (Copper-Silicon), J. Phase Equilibria Diffus. 33 (2012) 415–416, https://doi.org/10.1007/s11669-012-0076-2.

[41] A. Lama, R. Sarvesha, D. Garcia, T. Dolmetsch, T. Wang, R. Eberheim, K. Ross, A. Agarwal, Macroscale property assessment and indentation characteristics of thick section friction stir welded AA 5083, Mater. Sci. Eng. A 880 (2023) 145306, https://doi.org/10.1016/j.msea.2023.145306.

[42] T. Romano, M. Abdelwahed, S. Bengtsson, F. Bruzzo, R. Casati, H. Gedda, E. López, P. Ulfberg, C. Wilsnack, M. Vedani, Hybrid laser metal deposition of a Fe–Cr–Mo–V–Mn tool steel for hot stamping applications, Prog. Addit. Manuf. 8 (2023) 1241–1256, https://doi.org/10.1007/s40964-023-00396-w.

[43] M. Abdelwahed, S. Bengtsson, R. Casati, A. Larsson, S. Petrella, M. Vedani, Effect of water atomization on properties of type 4130 steel processed by L-PBF, Mater. Des. 210 (2021) 110085, https://doi.org/10.1016/j.matdes.2021.110085.

[44] M. Abdelwahed, R. Casati, A. Larsson, S. Petrella, S. Bengtsson, M. Vedani, On the recycling of water atomized powder and the effects on properties of L-PBF processed 4130 low-alloy steel, Mater 15 (2022) 336, https://doi.org/10.3390/ma15010336.

[45] A. Zafari, K. Xia, Laser powder bed fusion of ultrahigh strength Fe-Cu alloys using elemental powders, Addit. Manuf. 47 (2021) 102270, https://doi.org/10.1016/j.addma.2021.102270.

[46] A. Zafari, K. Xia, Nano/ultrafine grained immiscible Fe-Cu alloy with ultrahigh strength produced by selective laser melting, Mater. Res. Lett. 9 (2021) 247–254, https://doi.org/10.1080/21663831.2021.1884620.

[47] A. Munitz, Liquid separation effects in Fe-Cu alloys solidified under different cooling rates, Metall. Trans. B 18 (1987) 565–575, https://doi.org/10.1007/BF02654269.
[48] V.T. Witusiewicz, F. Sommer, E.J. Mittemeijer, Reevaluation of the Fe-Mn phase diagram, J. Phase Equilibria Diffus. 25 (2004) 346–354, https://doi.org/10.1361/15477030420115.
[49] L.T. Khajavi, M. Barati, Thermodynamics of phosphorus removal from silicon in solvent refining of silicon, High Temp. Mater. Process. 31 (2012) 627–631, https://doi.org/10.1515/htmp-2012-0100.
[50] N. Lu, Z. Lei, X. Yu, J. Bi, Y. Chen, Effects of melt convection on stray grain formation in single crystal superalloys during directed energy deposition, Addit. Manuf. 48 (2021) 102429, https://doi.org/10.1016/J.ADDMA.2021.102429.
[51] E. Sprague, J. Mazumder, A. Misra, Cooling rate and dendrite spacing control in direct metal deposition printed Cu-Fe alloys, J. Laser Appl. 34 (2022) 022013, https://doi.org/10.2351/7.0000464.
[52] C. Tan, Y. Chew, G. Bi, D. Wang, W. Ma, Y. Yang, K. Zhou, Additive manufacturing of steel–copper functionally graded material with ultrahigh bonding strength, J. Mater. Sci. Technol. 72 (2021) 217–222, https://doi.org/10.1016/j.jmst.2020.07.044.
[53] T. DebRoy, H.L. Wei, J.S. Zuback, T. Mukherjee, J.W. Elmer, J.O. Milewski, A. M. Beese, A. Wilson-Heid, A. De, W. Zhang, Additive manufacturing of metallic components – Process, structure and properties, Prog. Mater Sci. 92 (2018) 112–224, https://doi.org/10.1016/j.pmatsci.2017.10.001.
[54] G. Telasang, S. Narayanaswamy, R. Bathe, Selective laser melting of stainless steel on the copper alloy: an investigation of the interfacial microstructure and mechanical properties, J. Manuf. Process. 80 (2022) 920–929, https://doi.org/10.1016/j.jmapro.2022.06.055.
[55] S. Zhou, M. Xie, C. Wu, Y. Yi, D. Chen, L.C. Zhang, Selective laser melting of bulk immiscible alloy with enhanced strength: Heterogeneous microstructure and deformation mechanisms, J. Mater. Sci. Technol. 104 (2022) 81–87, https://doi.org/10.1016/j.jmst.2021.06.062.
[56] T. Xi, M. Babar Shahzad, D. Xu, J. Zhao, C. Yang, M. Qi, K. Yang, Copper precipitation behavior and mechanical properties of Cu-bearing 316L austenitic stainless steel: a comprehensive cross-correlation study, Mater. Sci. Eng. A 675 (2016) 243–252, https://doi.org/10.1016/j.msea.2016.08.058.
[57] L.A. Matlakhova, E.C. Pessanha, H. Alves, N.A. Palii, S.N. Monteiro, Phase composition and temperature effect on the dynamic Young's modulus, shear modulus, internal friction, and dilatometric changes in AISI 4130 steel, Crystals 13 (2023) 930, https://doi.org/10.3390/cryst13060930.
[58] S. Zhang, Q. Wang, R. Yang, C. Dong, Composition equivalents of stainless steels understood via gamma stabilizing efficiency, Sci. Rep. 11 (2021) 5423, https://doi.org/10.1038/s41598-021-84917-z.
[59] D. Ye, L. Yu, W. Jiang, K. Zhao, J. Su, Synergistic effect of Cu and Ni on the formation of reversed austenite in super martensitic stainless steel, Ironmak. Steelmak. 47 (2020) 381–387, https://doi.org/10.1080/03019233.2018.1522099.
[60] L. Ren, J. Zhu, L. Nan, K. Yang, Differential scanning calorimetry analysis on Cu precipitation in a high Cu austenitic stainless steel, Mater. Des. 32 (2011) 3980–3985, https://doi.org/10.1016/j.matdes.2011.03.068.
[61] A. Yadav, M. Srivastava, P.K. Jain, S. Rathee, Microstructure and tribological behaviour of dissimilar steel functional structure developed via arc-based DED process, Tribol. Int. 197 (2024) 109782, https://doi.org/10.1016/j.triboint.2024.109782.
[62] T.A. Rodrigues, N. Bairrão, F.W.C. Farias, A. Shamsolhodaei, J. Shen, N. Zhou, E. Maawad, N. Schell, T.G. Santos, J.P. Oliveira, Steel-copper functionally graded material produced by twin-wire and arc additive manufacturing (T-WAAM), Mater. Des. 213 (2022) 110270, https://doi.org/10.1016/j.matdes.2021.110270.
[63] N. Hutasoit, V. Luzin, A. Blicblau, W. Yan, M. Brandt, R. Cottam, Fatigue life of laser clad hardfacing alloys on AISI 4130 steel under rotary bending fatigue test, Int. J. Fatigue 72 (2015) 42–52, https://doi.org/10.1016/j.ijfatigue.2014.11.001.
[64] S.F. Hassan, K.F. Ho, M. Gupta, Increasing elastic modulus, strength and CTE of AZ91 by reinforcing pure magnesium with elemental copper, Mater. Lett. 58 (2004) 2143–2146, https://doi.org/10.1016/j.matlet.2004.01.011.
[65] J. Wilzer, J. Küpferle, S. Weber, W. Theisen, Influence of alloying elements, heat treatment, and temperature on the thermal conductivity of heat treatable steels, Steel Res. Int. 86 (2015) 1234–1241, https://doi.org/10.1002/srin.201400294.
[66] P. Koniorczyk, J. Zmywaczyk, A. Debski, M. Zielinski, M. Cegła, Investigations of thermal diffusivity and thermal expansion for three types of the barrel steel, AIP Conf. Proc. 2170 (2019) 020006, https://doi.org/10.1063/1.5132725.
[67] G. Benchabane, Z. Boumerzoug, I. Thibon, T. Gloriant, Recrystallization of pure copper investigated by calorimetry and microhardness, Mater Charact 59 (2008) 1425–1428, https://doi.org/10.1016/j.matchar.2008.01.002.
[68] S. Pan, T. Zheng, G. Yao, Y. Chi, I. De Rosa, X. Li, High-strength and high-conductivity in situ Cu–TiB2 nanocomposites, Mater. Sci. Eng. A 831 (2022) 141952, https://doi.org/10.1016/j.msea.2021.141952.
[69] H. Yang, K. Li, Y. Bu, J. Wu, Y. Fang, L. Meng, J. Liu, H. Wang, Nanoprecipitates induced dislocation pinning and multiplication strategy for designing high strength, plasticity and conductivity Cu alloys, Scr. Mater. 195 (2021) 113741, https://doi.org/10.1016/j.scriptamat.2021.113741.